Bayesian approach to the analysis of XENON100 data

Diplomarbeit in Physik

von

Stefan Schindler

vorgelegt dem Fachbereich Physik, Mathematik und Informatik (FB 08)
der Johannes Gutenberg-Universität Mainz

Juni 2013

1. Gutachter : Prof. Dr. Uwe Gerd Oberlack
2. Gutachter : Prof. Dr. Lutz Köpke

Contents

Introduction

Today we know that the universe is not that empty as believed earlier. But also only a small amount of the whole energy of the universe is made out of matter directly visible to us. The actual "standard model" of big bang cosmology is called Λ-Cold Dark Matter (ΛCDM)-Model, where Λ represents the cosmological constant. In this model our universe consists of 31.7 % matter and 68.3 % Dark Energy [1] (see section 1.1.3 for more details). The question what Dark Energy is stays a mystery and cannot be answered yet. Though its existence is needed to explain the observed accelerated expansion of the universe. Matter we can observe and interact with, is explained in the Standard Model of Particle Physics. Only about 4.9 %of the whole energy is made out of luminous and visible baryonic matter. The remaining amount (26.8 %) is of a yet not known kind, not directly visible to us and also seems to not interact with normal baryonic matter [1]. In the 1930 s, during his velocity observations of the Coma Cluster of galaxies, Fritz Zwicky [35] [36] was the first one who called it "dark" because of its non-luminous character and gave it its name: Dark Matter (DM). The Standard Model of Particle Physics provides no particles to explain the astronomical observations, so new and not yet known particles have to be found and the door to physics beyond the Standard Model is opened. The most promising particles, which arise from Supersymmetry (SUSY), an expansion to the Standard Model, are Weakly Interacting Massive Particles (WIMPs) (see section 1.1.4) wich are the Lightest Supersymmetric Particles (LSPs).

This work aims to introduce a new, alternative approach to analyze the data provided by the XENON100 Dark Matter project. To accomplish this, the need to understand the calculations behind the elastic scattering of WIMPs of a target nucleus is essential, the basics will be discussed in section 1.3. A `C++` program was developed to calculate the differential energy rates that also includes the XENON100 specific parameters and detector responses. The response of the XENON100 detector, a two phase Time Projection Chamber (TPC), and its Photomultiplier Tubes (PMTs) is studied in detail, see section 2.2 and section 4 where a simulation is done to estimate the average single photoelectron response width of the PMTs. Earlier analysis were done with the profile likelihood method, which uses a frequentist interpretation of probability. In this work Bayesian inference will be used to calculate Confidence Limits (CLs) for the cross-section of WIMP-nucleus interactions. In the Bayesian interpretation, probability is a "degree of believe" and together with Bayes' theorem a consistent way is provided to update these believes by calculating the posterior probability density function, see section 3.2. For the Bayesian analysis the Bayesian Analysis Toolkit (BAT), which is explained in section 3.3, is used. This software package provides the needed abilities, through Markov Chain Monte Carlo (MCMC) calculations, to obtain the posterior probability density function where numerical integration is needed.

1 Dark Matter

This chapter gives a motivation for introducing DM. With the help of astronomical observations the need of a new kind of matter is shown.

1.1 Evidence for Dark Matter

1.1.1 Rotational curves of spiral galaxies

Since the early 1930's many observations have shown that the velocities of stars in the outer parts of spiral galaxies are too high. With the given speed the stars would not remain on their orbits because the gravitational attraction is not strong enough to hold them in their paths around the galactic center (e.g. [30]). As an example, Fig. 1.1 shows data taken for galaxy NGC 6503.

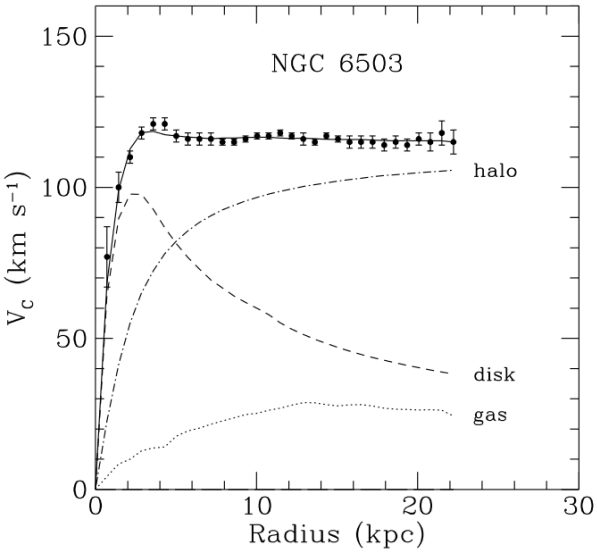

Figure 1.1.: The discrepancy between data and different models for the velocity distribution of stars in spiral galaxies is shown. The disk only-model (dashed line) does not fit the observed data (solid line with data points) [10].

First thing to notice is the huge discrepancy between the data points and the given model assuming a disk-only distribution of matter (with a spherical galactic bulge for $r < 4\,\mathrm{kpc}$). Newtonian dynamics predict a curve with decreasing velocity for increasing distance:

$$v \propto \frac{1}{\sqrt{r}}. \tag{1.1}$$

Even if the non-luminous gas (dotted line in 1.1), which makes up about 80 % of the galaxy's mass is taken into account, the observed roughly constant speed for an increasing radius can not be explained. If we assume Newtons gravitational law to apply even in these distances (alternative approach in section 1.2.1), a not yet discovered form of massive particles have to be present to hold the galaxy together and prevent it from being torn apart.

After introducing DM (dot-dashed line in Fig. 1.1) in form of a halo, the observed velocity distribution can be explained. A halo describes a spherical isotropic distribution of DM with its center in the nucleus of the galaxy.

1.1.2 Galaxy Clusters and Gravitational Lensing

As mentioned in the introduction, Fritz Zwicky was the first one to call the missing matter "dark" [35]. During his observations of the velocities of Galaxies in the Coma-Galaxy cluster, he discovered a discrepancy in the mass that was calculated through the luminosity of the galaxies and the mass calculated with the virial theorem $\bar{E}_{kin} = -\frac{1}{2}\bar{E}_{pot}$. The calculation with the virial theorem yielded a factor of 400 more mass. Later this factor was corrected to a smaller value with new measurements of the Hubble constant and by including the mass of the gas and dust (which makes up to 80 % of the mass of a galaxy) from the observations in different spectral ranges. This gas could not be bound to the galaxy with only the gravitational force from the stars. Even with this changes there was sill a lot of mass missing [36].

Another hint for DM can be found in the observation of two colliding galaxy clusters. A well-known example is the Bullet Cluster (see Fig. 1.2). Since there is a lot of space between the galaxies in the two clusters, the galaxies can pass each other without a collision. On the other hand, the intergalactic gas that is bound between the galaxies by gravitation, does collide and interacts with each other. As the gas of the galaxies collides, it heats up and emits X-radiation. This is indicated red in Fig. 1.2 while the mass distribution of the colliding galaxy clusters is colored blue. After the collision, the center of mass and the interstellar gas of the galaxies are found in different places. While the visible part (mostly gas) did collide, the center of mass is left almost untouched. This indicates a form of dark (not visible) matter in the clusters that does not interact as readily as the visible matter part.

Gravitational lensing is e.g. used to estimate the Bullet Cluster´s center of mass. Analogously to geometrical optics where light is bent at the transition of two media, light is bent in the presence of high masses (high gravitational potential) which is called gravitational lensing. Fig. 1.3 shows an illustration and Fig. 1.4 the observed effect. With the help of this effect the mass of massive astrophysical objects can be calculated.

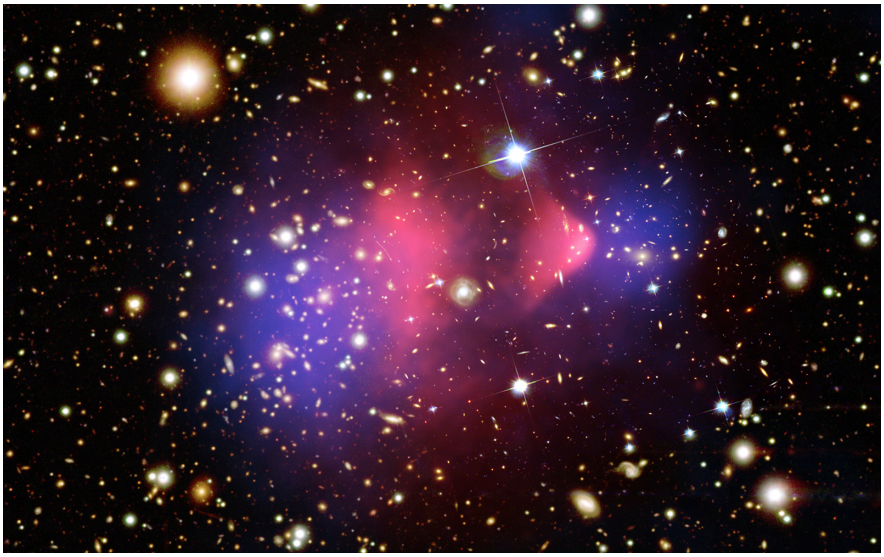

Figure 1.2.: The collision of two galaxy clusters formed the Bullet Cluster. The center of mass (blue) is left untouched, the gas collides and is heated up in this process (red) and forms the bullet cone shaped structure (on the middle right side) which is characteristic for this cluster [15].

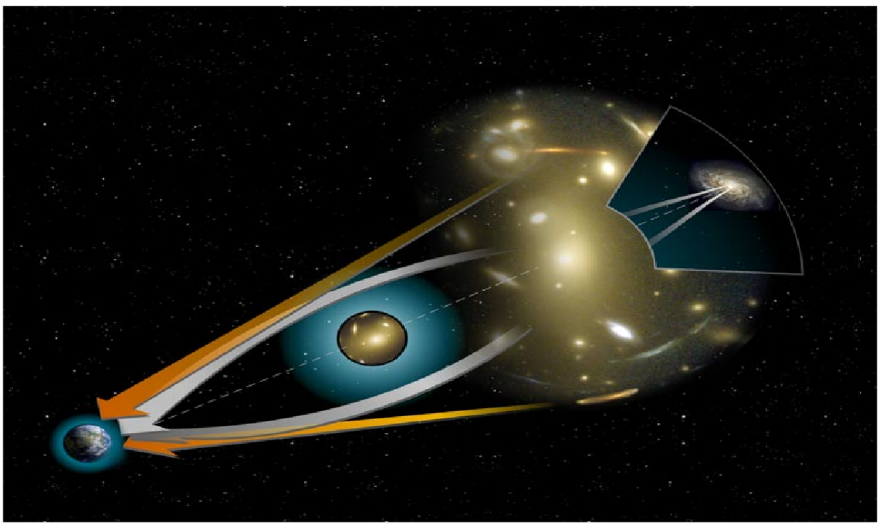

Figure 1.3.: Light is bent around massive objects analogously to refraction in optics (image courtesy of NASA).

1.1.3 Cosmic Microwave Background

In 1964 Arno Penzias and Robert Wilson discovered the Cosmic Microwave Background (CMB) [27]. As they were looking for radiation sources with their radio-telescope they observed some noisy background. This microwave radiation that corresponds

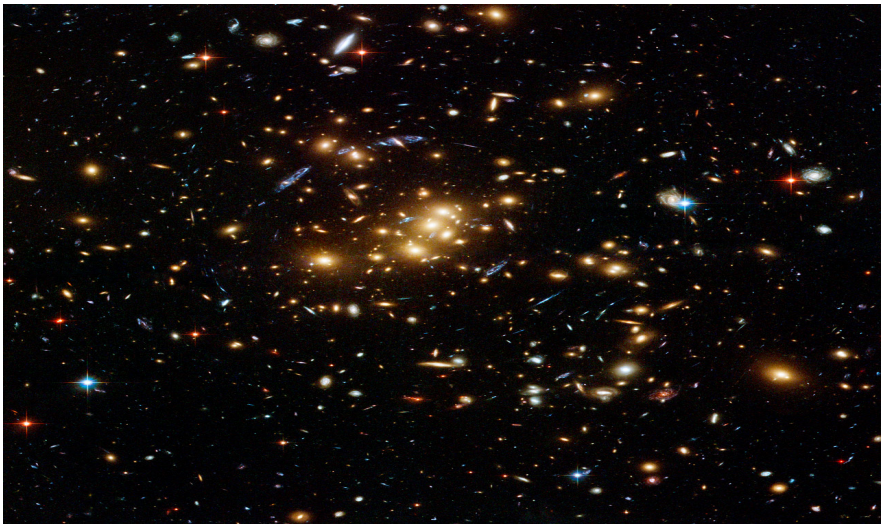

Figure 1.4.: Image of galaxy cluster Cl 0024+17 made by the Hubble space telescope. Faint far away galaxies (blue) have their light bent by the cluster's gravitational potential (yellow) (image courtesy of NASA & ESA).

to approximately 2.7 K came from every direction they were looking at. The CMB consists of photons that were emitted 380.000 years after the Big Bang. At this stage during the cooling-down of the early universe the photons no longer had enough energy to ionize hydrogen or helium, so the universe became transparent to those photons. Later CMB measurements with high precision by COBE, WMAP or just recently the Planck satellite revealed very small fluctuations in the highly uniform temperature (see Fig. 1.5). These fluctuations are in the order of 10^{-5} K and give us a picture of density fluctuations in the early universe. After decomposition into spherical harmonics a spatially correlation shows up (Fig. 1.6). Several peaks appear after plotting the temperature and polarization power spectrum. The ratio between these peaks can be used to estimate the composition of our universe. The CMB provides information about the densities of normal (baryonic) matter, Dark Matter and total energy density [1].

The best fitting theory for the obtained parameters is the ΛCDM-model, which is established as the standard model of Big Bang cosmology. In March 2013 the best fit of the new Planck power spectrum corrected the composition of the universe in the favor of even more DM. The baryonic part was nearly unchanged, as shown in Fig. 1.7. Only 4.9 % of the universe consists of baryonic matter, the main part (68.3 %) is Dark Energy of which almost nothing is known. About 26.8 % has to be "cold" Dark Matter of which no interaction with normal baryonic matter has been observed this far. It is called cold because the DM has to be non-relativistic, the kinetic energy of the particles should be low and thus also their speed ($v_{DM} << c$). Otherwise the structure of the universe would be different as observed today.

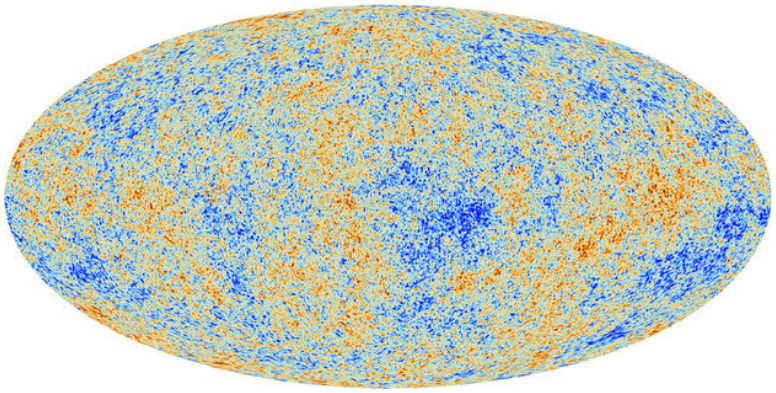

Figure 1.5.: Fluctuations in the temperature for the CMB from the recently published Planck satellite data [1]. The different colors correspond to temperature differences in the order of 10^{-5} K.

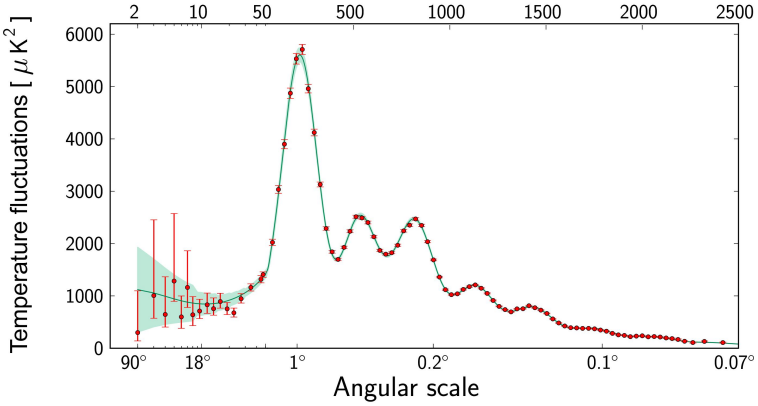

Figure 1.6.: Temperature and polarization power spectrum obtained from the Planck satellite. Points represent data, the red line corresponds to the best fit for the ΛCDM model [2].

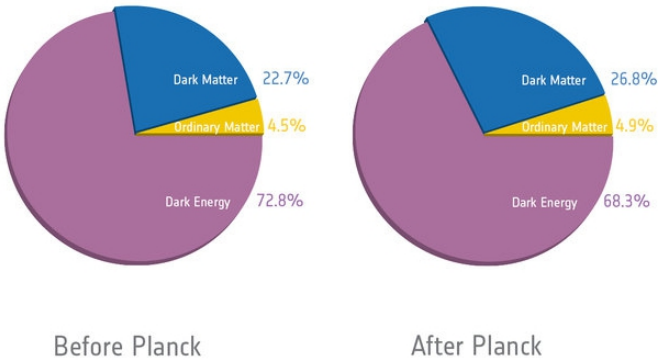

Figure 1.7.: Comparison of the composition of the Universe for 9 years of WMAP data [21] and the new Planck results [1].

1.1.4 Weakly Interacting Massive Particle

Even with all evidences observed so far, the nature of DM is still unknown. If DM would interact over the strong or electromagnetic force, it already should have been discovered. Electromagnetic interaction would cause photons to be scattered and/or absorbed by DM and therefore it should be visible to us to some extend. The strong force only affects baryonic matter and the primordial nucleosynthesis tells us what fraction of baryonic matter should be present compared to the whole energy of the universe [28]. It agrees very well with the results coming from the measurements of the CMB (see section 1.1.3). According to the ΛCDM model the fraction of matter should be about 30 % of the whole energy, so most of the matter has to be non-baryonic matter that cannot interact through the strong force exchanging gluons. Apart from gravitation there is only the weak force left to interact with DM.

No particle in the standard model of particle physics provides the needed characteristics of only interacting through the weak force and being massive (otherwise they should have already been detected in a collider experiment). Supersymmetry (SUSY) is a possible expansion to the Standard Model of Particle Physics that contains the needed particles. In SUSY every particle has its supersymmetric partner (every fermion gets a supersymmetric bosonic partner and vice versa). The partner can also have a different mass compared to the Standard Model particle (broken symmetry). The most promising candidate is the Weakly Interacting Massive Particle, which is the LSP.

If a SUSY particle cannot decay in normal particles there should be a stable LSP. There is still the problem, that if DM interacts weakly over the neutral current (exchanging a Z^0-boson), it also should have already been detected. If WIMPs are SUSY particles, the exchanging particles would also be supersymmetric particles. This would yield the expected small cross-section for the interaction of DM with normal baryonic matter [34].

1.2 Alternative Models

There are theories that do not introduce WIMP DM to solve the observed astrophysical discrepancies between theory and measured data. Only a few will be discussed here.

1.2.1 Modified Newtonian Dynamics (MOND)

In MOdified Newtonian Dynamics (MOND), no new kind of matter is introduced. Instead the gravitational law is modified. At first nobody wanted to believe in the existence of new particles, this rather abstract thought was rejected instead for astronomical distances a modification of the Newtonian dynamics was preferred. A new scale factor was introduced to Newtonian dynamics which modifies the gravitational force at long distances [26].

The rotation curves of spiral galaxies could be described with MOND and there would

be no need for DM. But even in this theory DM is necessary to describe the behavior of whole galaxy clusters. There are still theories like the TeVeS theory (Tensor-Vector-Scalar [9]), the relativistic extension of MOND, which aims to explain astrophysical observations without DM.

1.2.2 Massive Astrophysical Compact Halo Objects (MACHOs)

To avoid the introduction of DM there was also a search for not yet discovered non-luminous baryonic matter. Brown Dwarfs for example are small "light" stars which, due to their small masses, are not able to start fusion processes and therefore are dark. Other non-luminous objects are gas giants, like Jupiter. These objects are called Massive Astrophysical Compact Halo Objects (MACHOs). If there would be a high amount of these objects the missing mass could be explained. Even after an extensive search, the number of discovered MACHOs is not nearly high enough. In 2007 the EROS-2 project published results, where less then 8 % of the DM halo mass could be due to MACHOs [31]. Undiscovered MACHOs, like black holes, could provide the necessary mass to explain observed phenomena (velocities of spiral galaxies or the Bullet Cluster). But this is rather unexpected [32], especially as such objects consist of baryonic matter, which contradicts CMB results.

1.3 Direct Detection

With all the evidence shown before, we can assume that our planet moves through a halo of DM, so direct detection should be possible. There are different Models describing the distribution of DM in our galaxy. This work will focus on the "simple" Standard Halo Model (SHM) where it is assumed that we have an isotropic and spherical density distribution of DM in the Milky Way which is only dependent on the distance to the galactic center. As the galaxy is rotating, normal matter and dark matter is interpenetrating the whole time. Because of the very small cross-section the interaction rate is expected to be very low.

WIMPs are supposed to interact with normal matter by depositing a small amount of energy as they scatter elastically on target nuclei. To measure such small energies a detector with a very low background is needed. A lot of things like detector location, shielding and discrimination techniques have to be considered. Because of natural radioactivity and produced radiation, only very pure materials can be used and thus a lot of effort is put into selecting them.

The following sections will give an overview in how to calculate these rates (see [24] for reference if not mentioned different).

1.3.1 Standard Halo Model

Considering an isotropic and spherical density distribution of DM and the radial distance of our solar system in the galaxy, the local DM density is assumed to be

$$\rho_D \approx 0.3 \frac{\text{GeV}}{c^2 \cdot \text{cm}^3} \tag{1.2}$$

on and around earth [12]. For sure DM will not be stationary. To counter gravity and provide an equilibrium state it has to be in motion and will have a velocity distribution itself. A simple Maxwellian velocity distribution

$$f(\vec{v}, \vec{v}_e) = \exp\left[-\frac{(\vec{v} - \vec{v}_e)^2}{v_0^2}\right] \tag{1.3}$$

is assumed for this model where $\vec{v}$ is the WIMP velocity relative to the target and $\vec{v}_e$ is the velocity of earth ($\vec{v}$ represents the 3-dimensional velocity vector) and $v_0 = 230\,\text{km/s}$ is the normalization velocity. For the particle to be still bound in the gravitational potential of the galaxy the velocity is constrained. Above the escape velocity $v_{esc} = 544\,\frac{\text{km}}{\text{s}}$ particles are no longer bound and escape the galaxy. Because in the SHM the halo does not rotate, the mean of all velocities of the DM particles has to be zero. It should be noted that earth's velocity is not a constant because the earth moves around the sun while the sun moves around the galactic center. This annual modulation will not be considered in this work.

1.3.2 Scatter Rates and Spectra

To measure the rate of events R, a detector has to measure the recoil energy E_r that is deposited after an interaction. The outcome of the measurement therefore is the differential energy spectrum $\frac{\text{d}R}{\text{d}E_r}$. In general the recoil spectrum can be expressed as

$$\frac{\text{d}R}{\text{d}E_r} = R_0 \cdot S(E_r) \cdot F^2(E_r) \cdot I, \tag{1.4}$$

where R_0, see (1.11), is the unmodified rate if earth was stationary in the DM halo. $S(E_r)$ represents an energy-dependent factor which includes velocity effects, the detector thresholds or other instrumental dependencies. Since the interaction occurs with the target nucleus also the form factor $F(E_r)$ is needed. The spin of the interacting particles is considered with an additional factor I for spin dependent searches, which is not the case in this work.

1.3.3 Particle density and velocity distribution

The scatter rate for particles with density number n and uniform velocity v can be described by

$$R = \sigma n v \tag{1.5}$$

with the cross-section σ [25]. For a velocity distribution $f(\vec{v})$ of the incoming particles a differential scatter rate can be obtained with respect to $\mathrm{d}\vec{v}$:

$$\mathrm{d}R = \sigma n v \cdot f(\vec{v})\mathrm{d}^3 v = \sigma \cdot v \mathrm{d}n, \tag{1.6}$$

where $\mathrm{d}n$ is the differential particle density

$$\mathrm{d}n = \frac{n_0}{k} f(\vec{v})\mathrm{d}^3 v. \tag{1.7}$$

Here $n_0 = \rho/M_D$ is the local DM particle density for a WIMP of mass M_D in the laboratory frame and

$$k = \int_0^{2\pi} \mathrm{d}\Phi \cdot \int_{-1}^{1} \mathrm{d}\cos\Theta \cdot \int_0^{v_{esc}} f(\vec{v}) v^2 \mathrm{d}v \tag{1.8}$$

is a normalization factor such that

$$\int_0^{v_{esc}} \mathrm{d}n = n_0. \tag{1.9}$$

For a Maxwellian velocity distribution in the halo (see (1.3)) and a truncated velocity at $v = v_{esc}$, k can be written as

$$k = k_0 \left[\mathrm{erf}\left(\frac{v_{esc}}{v_0}\right) - \frac{2 \cdot v_{esc}}{\sqrt{\pi} \cdot v_0} \cdot \exp\left(\frac{-v_{esc}^2}{v_0^2}\right) \right], \tag{1.10}$$

with $k = k_0 = (\pi v_0^2)^{2/3}$ for $v_{esc} \mapsto \infty$. For earth velocity $v_e = 0$ and $v_{esc} \mapsto \infty$ the total scatter rate is

$$R_0 = \int_{v=0}^{\infty} \sigma \cdot v \mathrm{d}n = \frac{2}{\sqrt{\pi}} n_0 \sigma v_0. \tag{1.11}$$

For other velocities, $v_e \neq 0$, (1.6) yields

$$R = R_0 \frac{\sqrt{\pi}}{2} \frac{k_0}{k} \frac{1}{2\pi v_0^4} \int v f(\vec{v}) \mathrm{d}^3 v. \tag{1.12}$$

After integration of (1.12) in different ranges of the velocities - only WIMPs with a velocity of $v_e < v < v_{esc}$ can be detected in a target on earth - we get R with respect to v_e and v_{esc}:

$$\begin{aligned}
\frac{R(0, v_{esc})}{R_0} =& \frac{k_0}{k} \left[1 - \left(1 + \frac{v_{esc}^2}{v_0^2} \right) \exp\left(\frac{-v_{esc}^2}{v_0^2} \right) \right], \\
\frac{R(v_e, \infty)}{R_0} =& \frac{1}{2} \left[\sqrt{\pi} \left(\frac{v_e}{v_0} + \frac{1}{2} \frac{v_e^2}{v_0^2} \right) \mathrm{erf}\left(\frac{v_e}{v_0} \right) + \exp\left(\frac{-v_e^2}{v_0^2} \right) \right], \\
\frac{R(v_e, v_{esc})}{R_0} =& \frac{k_0}{k} \left[\frac{R(v_e, \infty)}{R_0} - \left(\frac{v_{esc}^2}{v_0^2} + \frac{1}{3} \frac{v_e^2}{v_0^2} + 1 \right) \exp\left(\frac{-v_{esc}^2}{v_0^2} \right) \right],
\end{aligned} \tag{1.13}$$

where erf is the error-function. The differential recoil energy rate can now be expressed in dependence of the recoil energy E_r:

$$\frac{\mathrm{d}R}{\mathrm{d}E_r} = \int_{E_{min}}^{E_{max}} \frac{1}{E_r}\mathrm{d}R(E) = \frac{1}{E_0 \cdot r}\int_{v_{min}}^{v_{max}} \frac{v_0^2}{v^2}\mathrm{d}R(v) \tag{1.14}$$

with the kinematic factor

$$r = \frac{4M_D M_T}{(M_D + M_T)^2} \tag{1.15}$$

where M_T is the mass of the target nucleus. The minimal DM particle velocity v_{min} corresponds to $E_{min} = E_r/r$ and $E_0 = \frac{1}{2}M_D v_0^2$. With this, E_{min} is the smallest energy to give a recoil energy E_r. Together with (1.6) we finally get the differential recoil rates for different velocities:

$$\frac{\mathrm{d}R(0, v_{esc})}{\mathrm{d}E_r} = \frac{k_0}{k}\frac{R_0}{E_0 \cdot r}\left(\exp\left(\frac{-E_r}{E_0 \cdot r}\right) - \exp\left(\frac{-v_{esc}^2}{v_0^2}\right)\right), \tag{1.16}$$

$$\frac{\mathrm{d}R(v_e, \infty)}{\mathrm{d}E_r} = \frac{R_0}{E_0 \cdot r}\frac{\sqrt{\pi}}{4}\frac{v_0}{v_e}\left[\mathrm{erf}\left(\frac{v_{min} + v_e}{v_0}\right) - \mathrm{erf}\left(\frac{v_{min} - v_e}{v_0}\right)\right], \tag{1.17}$$

$$\frac{\mathrm{d}R(v_e, v_{esc})}{\mathrm{d}E_r} = \frac{k_0}{k}\left[\frac{dR(v_e, \infty)}{dE_r} - \frac{R_0}{E_0 \cdot r}\exp\left(\frac{-v_{esc}^2}{v_0^2}\right)\right]. \tag{1.18}$$

Conventionally R_0 is normalized with standard numerical expressions, $\rho_D = 0.4\,\mathrm{GeV/c^2/cm^3}$ and $v_0 = 230\,\mathrm{km/s}$ and is expressed in the units events/kg/day:

$$R_0 = \frac{503}{M_D M_T}\left(\frac{\sigma_0}{1 \cdot 10^{-36}\,\mathrm{cm^2}}\right)\left(\frac{\rho_D}{0.4\,\mathrm{GeV/c^2/cm^3}}\right)\left(\frac{v_0}{230\,\mathrm{km/s}}\right) \tag{1.19}$$

with M_D, M_T in $\mathrm{GeV/c^2}$.

1.3.4 Form factor correction

With rising momentum transfer q the de Broglie wavelength $\lambda = h/q$ is no longer large compared to the target nuclear radius, resulting in a dropping cross-section. This is represented by the form factor that introduces a q-dependence to the cross-section:

$$\sigma(qr_n) = \sigma_0 \cdot F^2(qr_n) \tag{1.20}$$

where r_n is the effective nuclear radius. For large atomic masses, e.g. $A = 131$ for ^{131}Xe, this effect becomes quite significant. Therefore it is important to understand the form factor. Usually it is described as the Fourier transform of the charge density distribution of the target nucleus. There are different models to approximate $F(qr_n)$, a now common way to express the density profile was suggested by Helm [20]. He

described the nucleus with a solid core density and a Gaussian falling density on the outside, called the skin thickness. With this approximation the form factor is obtained:

$$F(qr_n) = 3 \cdot \frac{j_1(qr_n)}{qr_n} \cdot \exp\left(\frac{-(qs)^2}{2}\right) \tag{1.21}$$

where $j_1(qr_n)$ is the first order spherical Bessel function and $s = 1\,\text{fm}$ the skin thickness. An advantage of this formulation is the possibility to solve this equation analytically. Fig. 1.8 shows $F(qr_n)$ for different nuclei.

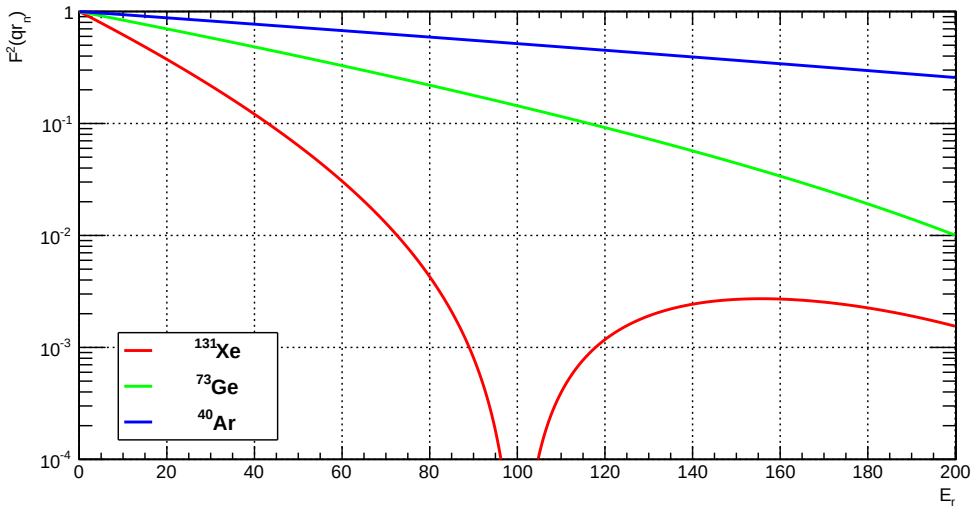

Figure 1.8.: Form factor for different target nuclei and recoil energies

1.3.5 Detector effects

Since no detector is perfect, some limitations are present and also corrections have to be made for obtaining the WIMP-nucleus recoil spectrum $\frac{\mathrm{d}R}{\mathrm{d}E_r}$. There are basically two key factors that alter the observed spectrum:

Energy detection efficiency

Especially at low energies the signal will drop below the noise level and therefore the efficiency drops to zero. There is also the possibility that a trigger does not capture 100 % of the events or that in data processing legitimate events are not taken into account. In the analysis some cuts could not be 100 % efficient in picking the events.

Energy resolution

Every detector has a finite energy resolution. In the XENON100 detector for example, low energies correspond to very few detected photoelectrons (see section 2 for more details and for conversion of photoelectrons to recoil energy). The resolution is dominated by Poisson counting statistics. Low recoil energies that normally would be below the energy threshold are only detectable because of statistical upward fluctuations. This helps with the detection of WIMPs with low masses which only produce a small signal, but it also broadens the spectrum for higher masses.

1.4 Indirect Detection

For indirect detection the aim is to detect particles produced after WIMP annihilations. There are a lot of different particles which could be produced in such an annihilation (e.g. neutrinos, γ-rays or anti-matter). It is quite challenging to verify that DM was the cause of the detected particles. Most of the produced particles would not make it to a detector located on earth because the atmosphere would absorb them. Only neutrinos are able to pass the atmosphere without any influence and can be detected.

For example, the IceCube neutrino telescope, located at the south pole, is searching for neutrino sources and might be able to detect neutrinos produced in the decay chain of WIMP annihilations [18]. Because, such neutrinos would have a high energy, they could be identified as a DM signal. Regions with a high amount of DM expected, like active galactic nuclei or stars, are interesting objects for the search of neutrinos produced by DM. Of course, IceCube is not only looking for neutrinos produced by DM. Its main goals are the search for supernovae and other extraterrestrial neutrino sources.

1.5 Production of WIMPs

The third way to study the nature of DM is the production in large particle colliders [16] [22]. Here particles which are forced to collide at high energies are supposed to produce WIMPs. With the corresponding center of mass energy and cross section the production theoretically should be possible. Since WIMPs only interact through the weak force, they can not be detected directly after the production. An indirect method based on the missing transverse energy respectively missing transverse momentum has to be used, like for the indirect detection of neutrinos which also only interact weakly.

2 The XENON100 detector

The XENON100 detector, located at the Laboratori Nazionali del Gran Sasso (LNGS) underground laboratory in Italy, is a two-phase Time Projection Chamber (TPC) with, as the name already suggests, liquid Xenon (LXe) as a detection medium. The detection chamber is about 30 cm in height and 30 cm in diameter (see Fig. 2.5a), the whole detector holds about 161 kg of LXe (with about 62 kg of active material and 99 kg for self-shielding and active veto) and is shielded by different passive materials (e.g. PTFE and copper, see Fig. 2.5b). LXe is sensitive to scintillation and ionization produced from particle interaction and both channels are used to get information about the deposited energy and nature of the particle interaction (electronic or nuclear recoil). It is also possible to do a 3-D position reconstruction, e.g. used to reduce the electromagnetic background from external sources by defining a fiducial volume [5]. With all its capabilities the XENON100 detector is currently the most sensitive experiment in direct search for WIMP Dark Matter. In this chapter we look at the detection principle of a TPC and also have a more detailed look in how the PMTs respond to a signal.

2.1 Xenon as a detection medium

In coherent scattering, the cross section is proportional to the square of the atomic mass number of the target nuclei A_T^2. Because of its high atomic number A and its high density, for low recoil energies and coherent scattering at the target nucleus, xenon yields the highest rates among the non-radioactive noble gases (see Fig. 2.1). On the other hand the rate drops more quickly than for lighter elements due to the form factor (as already shown on Fig. 1.8). Because the recoil energies are supposed to be very low, xenon is the optimal target material, in Fig. 2.2 the differential recoil energy spectra for different WIMP masses are shown. Also, what is very important (see section 2.2), electrons can drift almost with no resistance and xenon is a natural fast scintillator. On the cryogenic side LXe is also relatively easy to handle, it becomes liquid at -100 °C and can easily be cooled by e.g. a Pulse Tube Refrigerator (PTR).

2.1.1 Scintillation of LXe

There are two different reactions caused by a particle interaction (e.g. a WIMP) within LXe. The outcome of an interaction can be an excited state or the ionization of the Xe atom. Both, the excited and the ionized atom, react with surrounding neutral atoms creating excimers (excited dimers Xe_2^*) and dimers (Xe_2^+):

$$Xe^* + Xe \rightarrow Xe_2^*, \tag{2.1}$$

$$Xe^+ + Xe \rightarrow Xe_2^+. \tag{2.2}$$

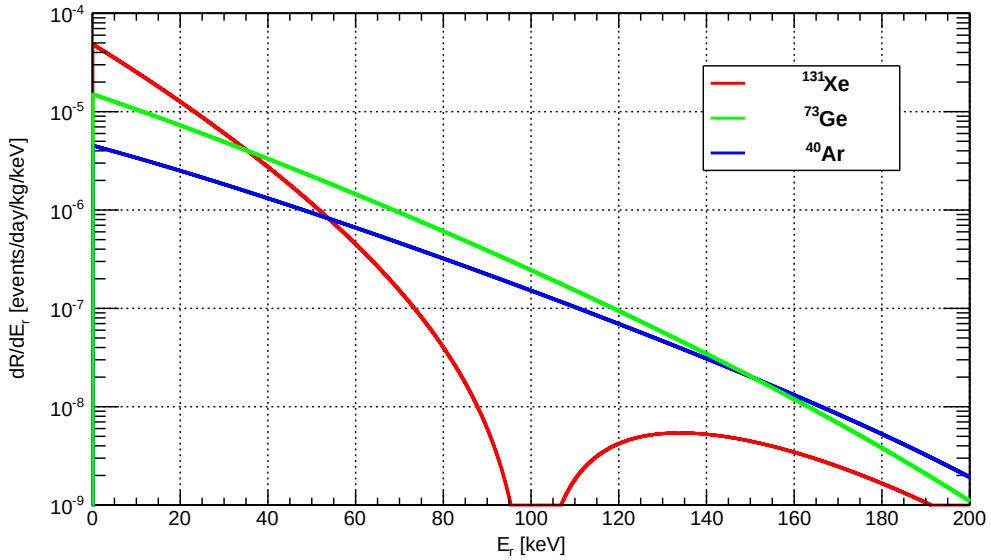

Figure 2.1.: Differential recoil energy spectra for ^{131}Xe, ^{73}Ge and ^{40}Ar for a WIMP of 100 GeV and a cross-section of 10^{-45} cm^2.

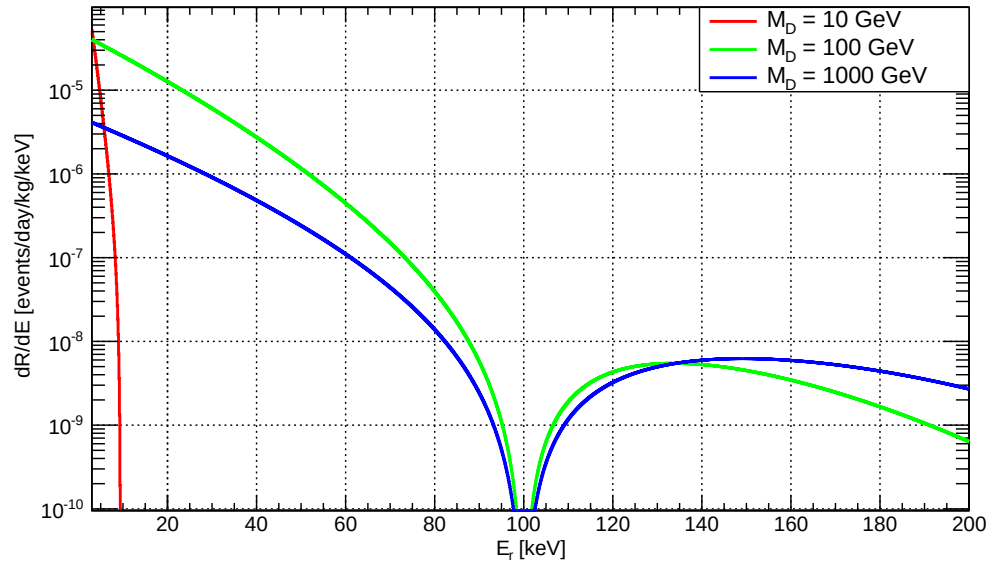

Figure 2.2.: Differential recoil energy spectra for different WIMP massses for a cross-section of $\sigma = 1 \cdot 10^{-45}$ cm^2.

The excimers decay by emitting VUV (vacuum-ultraviolet) radiation with a wavelength of 178 nm, for which xenon itself is transparent.

$$\mathrm{Xe}_2^* \rightarrow 2\ \mathrm{Xe} + h\nu \tag{2.3}$$

The dimers first recombine with the electrons from the earlier ionization and are reduced to excimers while producing heat and again, in the following disexcitation, light.

$$\mathrm{Xe}_2^+ + e^- \rightarrow \mathrm{Xe}_2^* + \mathrm{E}_{\mathrm{heat}} \tag{2.4}$$

The XENON100 detector is only sensitive to the VUV light, not to the produced heat.

2.2 Detection principle of the XENON100 Time Projection Chamber

Figure 2.3 shows the schematic buildup of a two-phase TPC like the XENON100 detector [5]. An incoming particle hitting the LXe induces a recoil leading to scintillation, producing photons and ionization electrons (see section 2.1.1). The produced photons hit the PMTs (which convert the photons into charge) where they are detected as the primary scintillation signal called $S1$. Between the two PMT arrays, one at the top

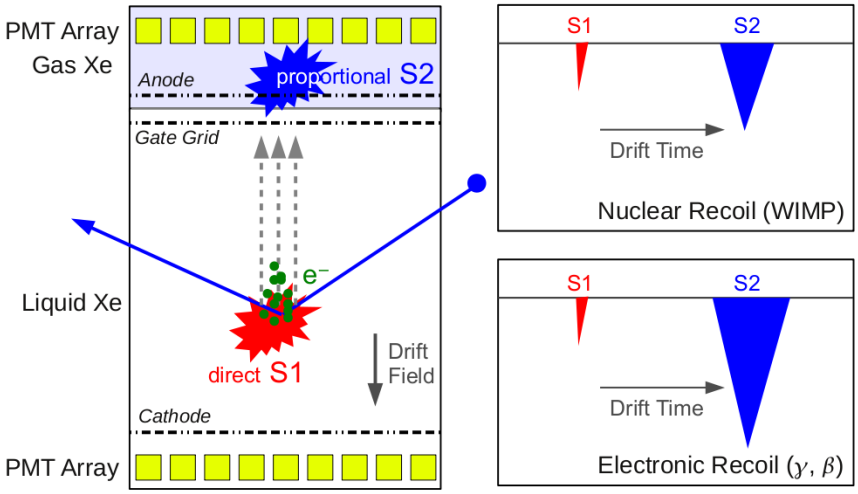

Figure 2.3.: Principle of an interaction inside the TPC producing primary scintillation light ($S1$) and proportional scintillation light ($S2$) (left) and the signals produced by different types of interaction (right) [5].

and one at the bottom (see Fig. 2.4a and 2.4b), the detection chamber is located. In this chamber between the anode and cathode meshes an electric field is applied. Not all electrons produced during the interaction recombine with the dimers and the electrons drift away from the interaction site because of the applied electrical field. The strength

of the field directly influences the amount of electrons which are able to drift away before recombination. The stronger the field the less excited dimers are there, which will produce light through disexcitation (see (2.4)). Therefore the strength of the field has to be chosen accordingly. The electrons are extracted into the gas phase when they reach the surface of the liquid phase. In the gaseous phase the electrons are accelerated because of the different relative permittivities and densities of liquid and gaseous xenon and also the additional electrical field between the gate grid and the anode mesh. The light produced and detected by the PMTs during this scintillation process is converted into another charge signal, the proportional scintillation signal $S2$.

Both signals, the direct scintillation light ($S1$) and the proportional scintillation light ($S2$), are detected with two PMT arrays. Because of the longer drift time of the electrons, compared to the fast photons, there is a time difference of the $S1$ and $S2$ signal. This is translated into the z-coordinate of the interaction position. The x-y-position is inferred by the proportional scintillation hit pattern on the top PMTs. The full reconstruction ability of the vertex allows the fiducialization of the target volume to e.g. further reduce background from double scatters, since WIMPs will only interact once.

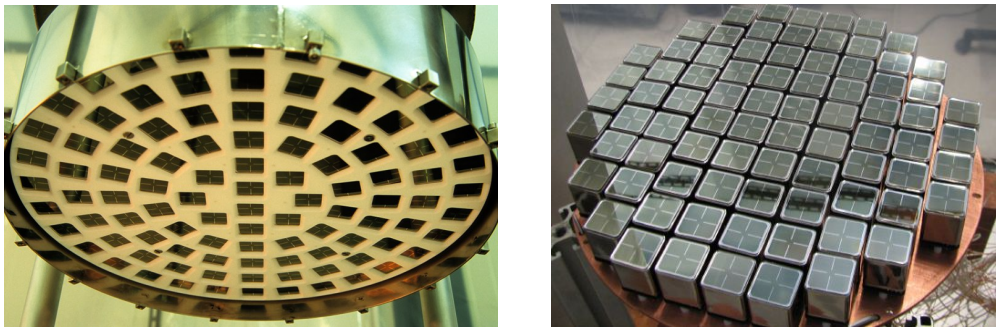

(a) Top array with 98 PMTs. **(b)** Bottom array with 80 PMTs.

Figure 2.4.: The 178 XENON100 PMTs divided into two arrays [5].

Different types of interactions, nuclear or electronic recoils, can be distinguished by the different ratios of $S2/S1$ (see right side of Fig. 2.3). Nuclear recoils are produced by neutrons or WIMPs (neutrons produce a WIMP-like signal which is capitalized for calibration). Electronic recoils are produced by γ- or β-radiation hitting the TPC. This provides an additional background discrimination possibility which depends on the deposited energy and the applied electrical field.

In the XENON100 detector additional discrimination is done with an active LXe veto system around the TPC chamber. The whole inner TPC is covered with LXe which provides good self-shielding. In Fig. 2.5a the XENON100 TPC is shown. Below and on top of the TPC chamber, which consists of PTFE because of good reflection capabilities of VUV scintillation light, are the PMT arrays. The visible rings of PMTs are the veto

PMTs sitting outside the active target volume inside the TPC.

In Fig. 2.5b the passive shield is shown. To reduce radioactivity from the walls and other surrounding sources the cryostat is locked in a shield consisting of different materials. The inner layer is made of 5 cm copper, followed by 20 cm of polyethylene and 20 cm of lead. Three sides of the shield are also covered with 20 cm of water to reduce the neutron background even further.

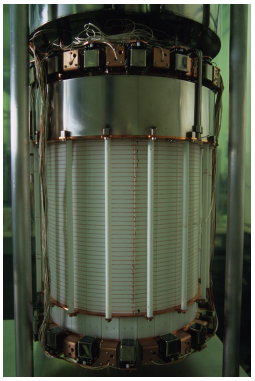

(a) Without any shielding. In the middle the mesh for the electrical field around the PTFE chamber can be seen.

(b) Inside the cryostat right in front of the passive shield.

Figure 2.5.: The XENON100 detector [5].

2.3 Measurement process

To be able to interpret the measured signal, the response of the PMTs has to be understood. More detailed information on the following elaborations can be found in [6]. Capital Latin letters in $S1$ and $S2$ are measured quantities, lowercase letters s1 and s2 represent the expectation values of the quantities. P will be a discrete probability and p is a probability density function (pdf).

The process of a WIMP hitting a target nucleus and producing light and charge, leading to the measured signals is described.

2.3.1 Generation of light and charge

The production of photons and electrons are independent statistical processes. Hence, the probability P can be described by independent Poisson processes:

$$P(N_\gamma, N_e|E_r, \mathcal{E}) \approx \mathrm{Poi}(N_\gamma|n_\gamma)\mathrm{Poi}(N_e|n_e), \tag{2.5}$$

where E_r corresponds to either nuclear or electronic recoil energies. $\mathcal{E}$ is the strength of the applied drift field, N_γ, N_e are the number of the generated photons and electrons, n_γ and n_e represent their expectation values.

Effective values express the average energies needed to create a photon or an electron. These values are called W-values, which depend on the interaction type, the electrical drift field in the TPC and on the deposited energy. Due to field quenching the light yield is reduced, which is expressed with a function S_r; T_r considers the loss of charge due to recombination. The expectation values can be rewritten to

$$n_\gamma(E_r, \mathcal{E}) \approx \frac{E_r}{W_\gamma(E_r, \mathcal{E}=0)} S_r(\mathcal{E}) \tag{2.6}$$

$$n_e(E_r, \mathcal{E}) \approx \frac{E_r}{W_e(E_r, \mathcal{E}_{ref} \to \infty)} T_r(\mathcal{E}) \tag{2.7}$$

where $S_r(0) = 1$ and $T_r(\infty) = 1$. For energy calibration, signals of known γ sources are used to compare dedicated measurements of the functions W_γ, S_r and W_e, T_r. For nuclear recoils (WIMP like signal) W_γ has been measured to lower energies and therefore the primary scintillation light is used to estimate the energy scale of the XENON100 detector.

2.3.2 Primary scintillation light ($S1$)

To get the full charge produced by a $S1$ signal the pulse is integrated. After integration the expectation value for the primary scintillation light on PMT$_i$ (i stands for one of the 180 PMTs) in units of photoelectrons (p.e.) with position dependent light detection efficiency factor $\mu_i(\vec{r})$ is given by

$$s1_i(\vec{r}) \approx n_\gamma(E_r, \mathcal{E}) \mu_i(\vec{r}). \tag{2.8}$$

It is position dependent because not every PMT sees the same amount of light of an interaction, which has to be corrected. Nuclear recoils that deposit an energy E_{nr} produce a total primary scintillation signal s1

$$s1(\vec{r}) = \sum_{i=1}^{M} s1_i(\vec{r}) \approx n_\gamma(E_{nr}, \mathcal{E}) \mu(\vec{r}) \tag{2.9}$$

$$= E_{nr} \mathcal{L}_y(E_{ee} = E_{ref}, \mathcal{E}, \vec{r}) \times \mathcal{L}_{eff}(E_{nr}, \mathcal{E}=0) \frac{S_{nr}(\mathcal{E})}{S_{ee}(\mathcal{E})} \tag{2.10}$$

for a number of M PMTs and $\sum_i \mu_i(\vec{r}) = \mu(\vec{r})$. S_{ee} and S_{nr} are field quenching factors and represent the reduction in light yield for nuclear (nr) or electronic (ee) recoils. For a reference γ-ray line, historically the 122 keV$_{ee}$ line of the ^{57}Co decay (ee $\widehat{=}$ electronic-equivalent recoil energy), $\mathcal{L}_y$ is the measured light yield in PE/keV$_{ee}$ for given electric field and position:

$$\mathcal{L}_y(E_{ee} = E_{ref}, \mathcal{E}, \vec{r}) = \frac{S_{ee}(\mathcal{E}) \mu(\vec{r})}{W_\gamma(E_{ee} = E_{ref}, \mathcal{E}=0)}. \tag{2.11}$$

The relative scintillation yield of nuclear recoils, with respect to the reference γ line and zero field, is called $\mathcal{L}_{eff}$ (see also Fig. 2.6):

$$\mathcal{L}_{eff}(E_{nr}, \mathcal{E} = 0) = \frac{W_\gamma(E_{ee} = E_{ref}, \mathcal{E} = 0)}{W_\gamma(E_{nr}, \mathcal{E} = 0)} \tag{2.12}$$

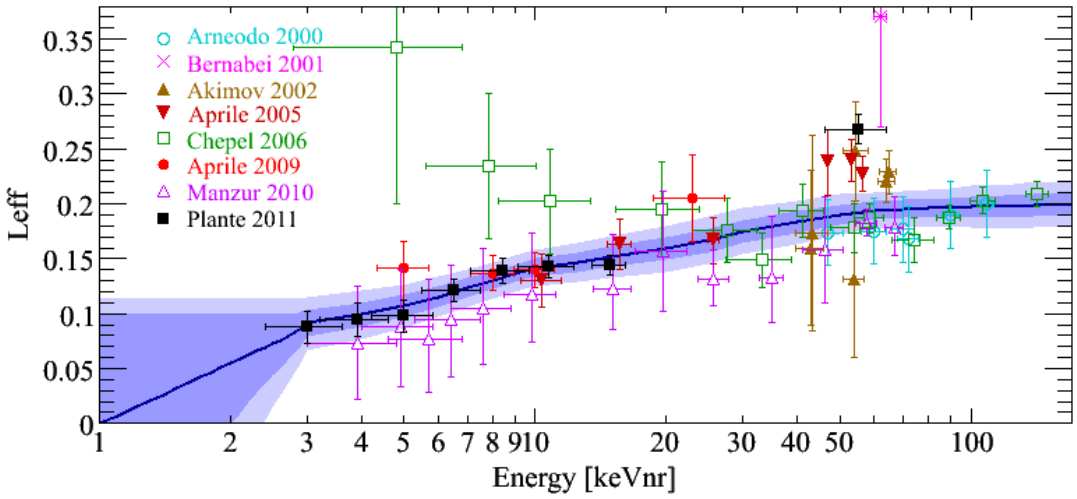

Figure 2.6.: Measured relative scintillation yield of nuclear recoils $\mathcal{L}_{eff}$ in dependence of the recoil energy E_{nr} [29].

After position correction is applied, the spatially-corrected $cS1$ is obtained. With this corrected value the analysis is usually done. Finally we get the detector-averaged signal expectation value:

$$cs1 = E_{nr} \langle L_y \rangle \mathcal{L}_{eff} \frac{S_{nr}}{S_{ee}} \tag{2.13}$$

where $\langle L_y \rangle$ is the average detector light yield. With this equation, it is now possible to convert the measured nuclear recoil energy E_{nr} into p.e. ($S1$). In Fig. 2.7 the direct conversion is shown. Below 3 keV, because of the uncertainty of $\mathcal{L}_{eff}$, the conversion only works with an extrapolation wich is modeled to drop to zero below 1 keV.

The generated photons N_γ are supposed to follow a Poisson distribution, the photo-electrons $N_{pe,i}$ produced in PMT$_i$ follow a binomial distribution. The pdf can then be

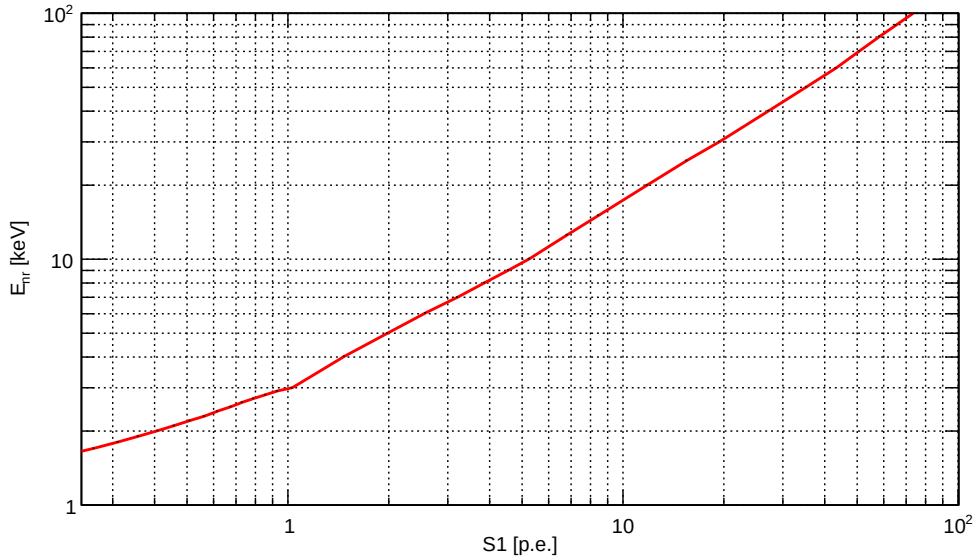

Figure 2.7.: Conversion of nuclear recoil energy E_{nr} to photoelectrons p.e. ($S1$) with (2.13) given.

described by:

$$\begin{aligned} p_{S1,i}(S1_i|n_\gamma(E_r,\mathcal{E}))\mathrm{d}S1_i &= \sum_{N_{pe,i}}\sum_{N_\gamma} p_{pmt,i}(S1_i|N_{pe,i})\mathrm{d}S1_i \\ &\quad \times \mathrm{Binom}(N_{pe,i}|N_\gamma,\mu_i(\vec{r})) \\ &\quad \times \mathrm{Poi}(N_\gamma|n_\gamma(E_r,\mathcal{E})) \\ &= \sum_{N_{pe,i}} p_{pmt,i}(S1_i|N_{pe,i}) \times \mathrm{Poi}(N_{pe,i}|n_\gamma\mu_i(\vec{r}))\mathrm{d}S1_i, \end{aligned} \tag{2.14}$$

where $p_{pmt,i}$ is the response of PMT$_i$ described by a Gaussian of mean value $N_{pe,i}$ and width $\sigma_{PMT_i}\cdot\sqrt{N_{pe,i}}$. The average single-photoelectron width σ_{PMT_i} is a PMT specific value which is determined through PMT calibrations.

Summing up to a total light signal $S1 = \sum_{i=1}^{M} S1_i$ and assuming an average response (measured through detector calibrations) of $\sigma_{PMT} = 0.5$ for all PMTs (2.14) can be written as:

$$p_{cS1}(cS1|n_\gamma(E_r,\mathcal{E}))\mathrm{d}cS1 \approx \sum_{N_{pe}} p_{pmt}(cS1|N_{pe}) \times \mathrm{Poi}(N_{pe}|\langle\mu\rangle n_\gamma)\mathrm{d}cS1, \tag{2.15}$$

where $N_{pe} = \sum_i N_{pe,i}$ is the sum of all photoelectrons released on all the PMTs. $p_{pmt}(cS1|N_{pe})$ has been modeled with the single photoelectron (SPE) response of a single PMT, i.e.

$$p_{pmt}(cS1|N_{pe}) \approx \sigma_{pmt}\cdot\sqrt{N_{p.e.}} \tag{2.16}$$

with $\sigma_{PMT} = 0.5$. The validity of this approach will be studied in section 4.

2.3.3 Proportional scintillation light ($S2$)

Electrons, produced at the point of interaction, drift through the liquid xenon towards the top PMT array because of the applied electric field. Due to impurities, characteristic losses occur. At the surface of the liquid phase, extraction into the gas phase depending on the applied extraction field takes place. In the gas phase the electrons are further accelerated and produce the proportional scintillation light $S2$ and the resulting scattering with gas atoms.

Considering all effects the secondary scintillation signal for nuclear recoils can be expressed as:

$$s2(\vec{r}) = E_r \cdot Q_y(E_r) e^{-t_d/\tau_e} \delta(x, y), \tag{2.17}$$

where Q_y (see also Fig. 2.8) is the charge yield of nuclear recoils at given electric field, the exponential function represents the losses due to impurities. $\delta(x, y)$ includes the probability which PMT can be reached by a photon, created in the gas gap at position (x,y). There is no z dependence because the gap is small ($\sim$2.5 mm) compared to the (x,y)-plane. It also contains corrections for scintillation gain, gas density and quantum efficiencies of the PMTs. Analogously to the pdf of the $S1$ signal (see (2.15)) we assume a Poisson distributed production of photons N_γ and a binomial distributed production of photoelectrons N_{pe} for every PMT:

$$p_{cS2}(cS2|n_e(E_r, \mathcal{E}))\mathrm{d}cS2 = \sum_{N_{pe}} p_{pmt}(cS2|N_{pe}) \times \mathrm{Poi}(N_{pe}|n_e\delta(x, y))\mathrm{d}cS2, \tag{2.18}$$

where p_{pmt} is the same response as in the case for the $S1$ signal [6].

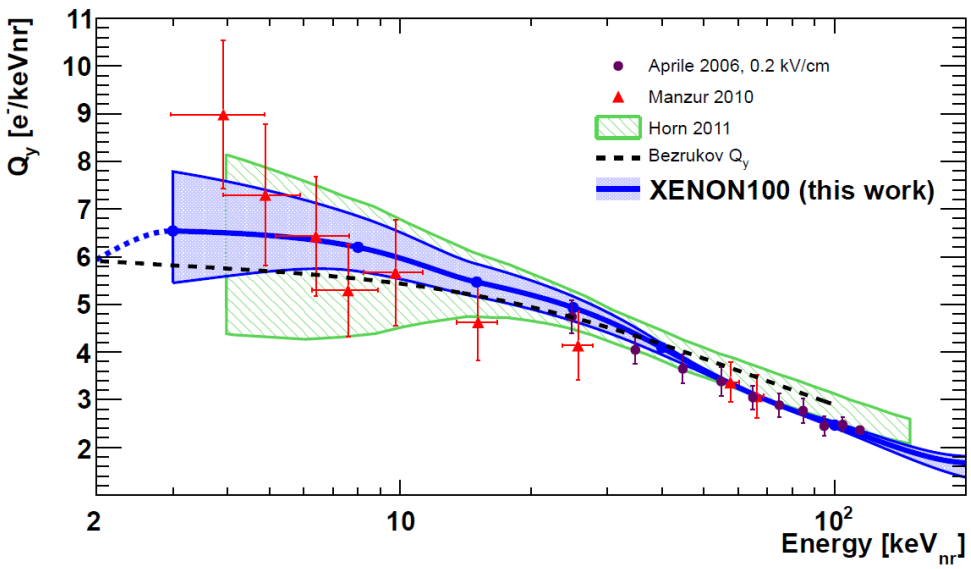

Figure 2.8.: Measured $Q_y(E_r)$ in dependence of the recoil energy E_{nr} [8].

2.4 Event Rate calculation

With a given WIMP-nucleus scattering rate $\mathrm{d}R/\mathrm{d}E_{nr}$ (1.18) the measured differential nuclear recoil rate is calculated as

$$\begin{aligned}\frac{\mathrm{d}^2R}{\mathrm{d}S1\,\mathrm{d}S2} &= \epsilon(S1,S2)\int \frac{\mathrm{d}R}{\mathrm{d}E_{nr}} p(S1,S2|E_{nr})\mathrm{d}E_{nr} \\ &\approx \epsilon_1(S1)\epsilon_2(S2)\int \frac{\mathrm{d}R}{\mathrm{d}E_{nr}} p_{S1}(S1|E_{nr})p_{S2}(S2|E_{nr})\mathrm{d}E_{nr} \end{aligned} \tag{2.19}$$

where $\epsilon_1(S1)$ is the combined cut acceptance coming from e.g. the different quality cuts in data selection also used in the Profile Likelihood (PL) analysis [4]. $\epsilon_2(S2)$ is the $S2$ threshold cut which represents the trigger threshold for a valid event to be above $S2 = 150\,\mathrm{p.e.}$ in run 10 of the XENON100 detector (see Fig. 2.9). These acceptances are obtained during calibration measurements of the XENON100 detector.

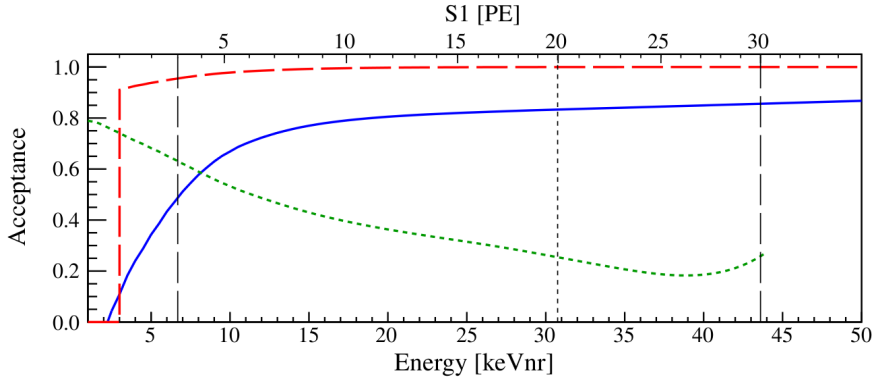

Figure 2.9.: Combined cut acceptance (solid blue line) and $S2$ threshold cut acceptance (dashed red line). The $S2$ threshold cut acceptance set to 0 below 1 p.e. [7]. The green dashed line is not from interest here.

The $S2$ threshold cut directly influences the $S1$ signal and has to be applied before considering the Poisson distributed energy resolution. The relation between E_{nr} and $S1$ has been measured more precisely and to lower energies via $\mathcal{L}_{eff}$ than the relation between E_{nr} and $S2$ via Q_y, see Fig. 2.6 and 2.8.

This is also the reason the analysis is done only with the measured differential rate expressed in the $S1$ signal. The two dimensional data space is reduced to be only dependent on the $S1$ signal:

$$\begin{aligned}\frac{\mathrm{d}R}{\mathrm{d}cS1} &\approx \epsilon_1(cS1)\int \frac{\mathrm{d}R}{\mathrm{d}E_{nr}} p_{cS1}(cS1|E_{nr}) \underbrace{\int_{S2_{min}} \epsilon_2(S2)p_{S2}(S2|E_{nr})\mathrm{d}S2}_{\epsilon_2(E_{nr}\propto cs1)}\,\mathrm{d}E_{nr}, \\ &= \epsilon_1(cS1)\int \frac{\mathrm{d}R}{\mathrm{d}E_{nr}} \epsilon_2(E_{nr})p_{cS1}(cS1|E_{nr})\mathrm{d}E_{nr}. \end{aligned} \tag{2.20}$$

We now have all it takes to calculate the expected rates of DM interactions in the XENON100 detector. The rates for a given reference cross-section $\sigma_{ref} = 10^{-45}\,\mathrm{cm}^2$ are calculated because they depend linearly on the cross-section $\frac{\mathrm{d}R}{\mathrm{d}cS1} \propto \sigma$. By multiplying a factor of σ_χ/σ_{ref} the reference cross-section can be canceled out in later calculations:

$$\frac{\sigma_\chi}{\sigma_{ref}} \cdot \frac{\mathrm{d}R(m_\chi, \sigma_{ref})}{\mathrm{d}cS1} = \frac{\mathrm{d}R(m_\chi, \sigma_\chi)}{\mathrm{d}cS1}. \tag{2.21}$$

With this, the rates for different WIMP masses only need to be calculated once, which is a huge advantage for later programming, because the cross-section will be the only free parameter in the beginning (see section 3.2).

3 Bayesian Inference

Basically there are two main approaches to statistics. The frequentist, or usual called classical approach and the Bayesian approach. Because Bayesian calculations can be quite complicated it was not a favored approach due to the lack of computing power for e.g. numerical integration. In the last 20 years rising computing power made it possible to do calculations that would have been impractical earlier. This led to a rapidly growing interest in Bayesian statistics. In this chapter the the basic philosophical differences between these two approaches are shown, Bayes' theorem is derived and established and the framework used for future studies, the Bayesian Analysis Toolkit [13], is introduced. For reference see [11] if not mentioned otherwise.

3.1 Frequentist approach

This way of looking at probability is the common way and is usually the first way to get to know statistics. The main ideas of this approach are:

- The parameters are fixed but unknown constants. They represent the numerical characteristics of the observed population.
- The interpretation of probability is always a long run relative frequency.
- The performance of statistical procedures is determined in the long run over an infinite number of hypothetical repetitions of an experiment.

Because the unknown parameters are fixed no statement about their probability can be made. Only for random quantities probability statements can be done about their values. A sample statistic is needed, by drawing samples out of the population. The probability distribution over all possible random samples of the population is determined (sampling distribution). The parameter of the population will also be a parameter of the sampling distribution. A confidence statement about the parameter can be made, which is based on the average behavior of the procedure under all possible samples, by converting the probability statement about the statistic based on its sampling distribution.

3.2 Bayesian interpretation of probability

The basis of the Bayesian approach is formed by the following ideas [11]:

- The parameters themselves are random variables due to the uncertainty about their true value.

- Inferences about the parameters are made by directly apply the rules of probability.
- Statements about the probability of a parameter must be interpreted as "degree of belief". The prior distribution must be subjective.
- Every person can have their own priors, considering different weights people give to the values of the parameters. This measures the plausibility each person gives a parameter value before observing the data.
- Revision in beliefs about parameters after getting the data is done using Bayes'theorem. This leads to the posterior distribution, which comes from two sources: the prior distribution and observation of the data.

With this method there is a consistent way of updating the beliefs about the parameters by looking at given data that was actually measured. So the inference, not like in the frequentist approach, is based on the data that actually happened and not on all possible data sets that might have occurred or not. With the actual data given there is nothing random left with a fixed parameter. Also the handling of nuisance parameters (parameters of which no inference is made about but influence on the main parameters has to be eliminated) is done in a general way. Bayesian statistics is predictive, there is a way to easily find the conditional probability distribution of the next observation given the sample data.

3.2.1 Conditional probability and Bayes'theorem

Consider two events, A and B, in the universe U. If event A has occurred what influence is there on the probability that event B can occur? To answer this we have to look at conditional probabilities. Assume event A has occurred, so everything outside A is no longer possible, the universe U has been reduced to $U_r = A$. Now, only the part of B that also lies in A, $A \cap B$ can occur (see Fig. 3.1a).

The probability of B given A is the unconditional probability of the part of B that is also in A multiplied by a scale factor $1/P(A)$ because the total probability in the reduced universe U_r has to be 1. This leads to the conditional probability of B given A:

$$P(B|A) = \frac{P(A \cap B)}{P(A)}. \tag{3.1}$$

With the conditional probability given and knowing that for independent events $P(B \cap A) = P(A) \times P(B)$ we can also write (3.1) as

$$P(B|A) = P(B). \tag{3.2}$$

So if A and B are independent, the probability of B occurring is not affected by knowledge of A. For sure, things could be turned around, so the result of A given B would be

$$P(A|B) = \frac{P(A \cap B)}{P(B)}. \tag{3.3}$$

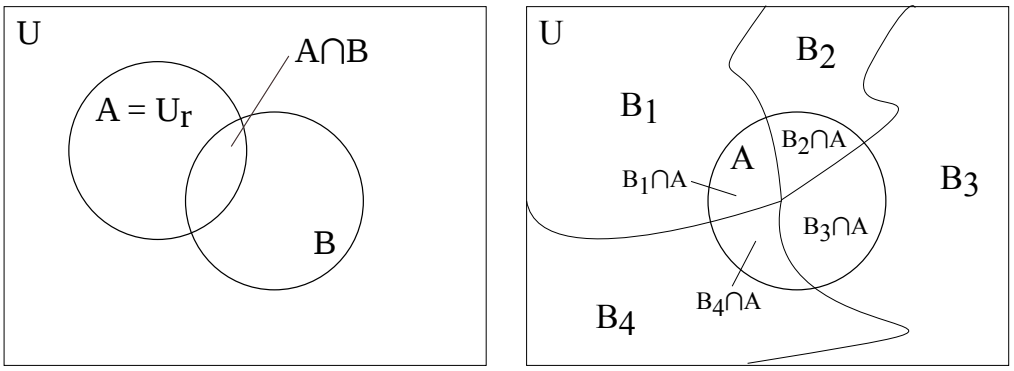

(a) Universe U reduced by Event A. Only parts of B also lying in A can occur.

(b) Universe U devided by $n = 4$ events. Only parts of B_i (where $i = 1, \ldots, 4$) also lying in A can occur.

Figure 3.1.: Conditional probability (own drawings).

However, the conditions on A and B can be different. Assume B is an unobservable event, so there is nothing known about the occurrence or nonoccurrence of B. A on the other hand is an observable event that can either occur with B or its complement $\bar{B}$. The probability that A occurs may depend on the occurrence of B or $\bar{B}$. After clearing the fractions, (3.1) leads to the relationship for conditional probability of an observable event given an unobservable finding the joint probabilities

$$P(A \cap B) = P(B) \times P(A|B) \text{ and} \tag{3.4}$$

$$P(A \cap \bar{B}) = P(\bar{B}) \times P(A|\bar{B}). \tag{3.5}$$

This is also called the multiplication rule for probability. With conditional probability in mind, it is known that the marginal probability of event A is the sum over its disjoint parts:

$$P(A) = P(A \cap B) + P(A \cap \bar{B}). \tag{3.6}$$

Substituting this into (3.1) yields:

$$P(B|A) = \frac{P(A \cap B)}{P(A \cap B) + P(A \cap \bar{B})}. \tag{3.7}$$

Now, using the multiplication rule from (3.4) and (3.5) the final result is called *Bayes' theorem* for a single event:

$$P(B|A) = \frac{P(A|B) \times P(B)}{P(A|B) \times P(B) + P(A|\bar{B}) \times P(\bar{B})}. \tag{3.8}$$

The two events B and $\bar{B}$ partition the universe, since $B \cup \bar{B} = U$ but also the events itself are distinct. Bayes' theorem can be generalized to n events, dividing the universe

into n parts ($B_1 \cup B_2 \cdots \cup B_n = U$ and $B_i \cap B_j = \emptyset$ for $i \neq j$), see also Fig. 3.1b:

$$P(B_i|A) = \frac{P(A|B_i) \times P(B_i)}{\sum_{j=1}^{n} P(A|B_j) \times P(B_j)}. \tag{3.9}$$

This is Bayes' theorem as published posthumously in 1763, named after its discoverer Thomas Bayes, an English mathematician and Presbyterian minister.

3.2.2 Bayes' theorem for parameter estimation

For later use we identify the different parts of Bayes' theorem to match our problem. It will be used do estimate the parameters to match a measured data set or, in other words, the probability of the parameters $\vec{\Theta}$ given the data X, the *posterior* probability:

$$\mathcal{P}(\vec{\Theta}|X) = \frac{\mathcal{L}(X|\vec{\Theta}) \cdot \pi(X)}{\int \mathcal{L}(X|\vec{\Theta}) \cdot \pi(X) \mathrm{d}\vec{\Theta}}. \tag{3.10}$$

It equals the probability of the data given the parameters $\mathcal{L}(X|\vec{\Theta})$, the *likelihood*, times the initial probability of the parameters $\pi(X)$, the *prior* probability. It is normalized by the integral of the likelihood times the prior probability over the allowed range of all parameters, $\int \mathcal{L}(X|\vec{\Theta}) \cdot \pi(X) \mathrm{d}\vec{\Theta}$ [13]. Note that now continuous values are assumed, resulting in the integral in (3.10) instead of the sum in (3.9).

It can be considered as a process of learning, as the prior knowledge about the parameters is updated in the light of new data gathered resulting in posterior knowledge (see Fig. 3.2 for illustration). The likelihood function and prior probability used for the later calculations will be introduced in Chapter 5.2.3.

The handling of nuisance parameters in Bayesian inference is quite simple an also straight forward. In the process of sampling with MCMC the parameters are integrated out. Let

$$\pi(\vec{\Theta}, \vec{\lambda}) = \pi(\vec{\Theta})\pi(\vec{\lambda}|\vec{\Theta}) \tag{3.11}$$

be the prior pdf. The inference then will be based on the marginal posterior of $\vec{\Theta}$ given the data X:

$$\mathcal{P}(\vec{\Theta}|X) = \frac{\pi(\vec{\Theta}) \int_{\vec{\lambda}} \mathcal{L}(\vec{\Theta}, \vec{\lambda}) \pi(\vec{\lambda}, \vec{\Theta}) \mathrm{d}\vec{\lambda}}{\int_{\vec{\Theta},\vec{\lambda}} \mathcal{L}(\vec{\Theta}, \vec{\lambda}) \pi(\vec{\Theta})) \pi(\vec{\lambda}, \vec{\Theta}) \mathrm{d}\vec{\lambda} \mathrm{d}\vec{\Theta}}. \tag{3.12}$$

This "tool" allows a large dimension of the nuisance parameter to make inference on the parameter from interest $\vec{\Theta}$ which can be multidimensional itself.

3.3 BAT - Bayesian Analysis Toolkit

The BAT software, coded in C++, is a framework, coming in form of a library [13]. It provides a flexible interface for model implementation, and a fast code for numerical calculations like maximization, marginalization and integration. It has interfaces to

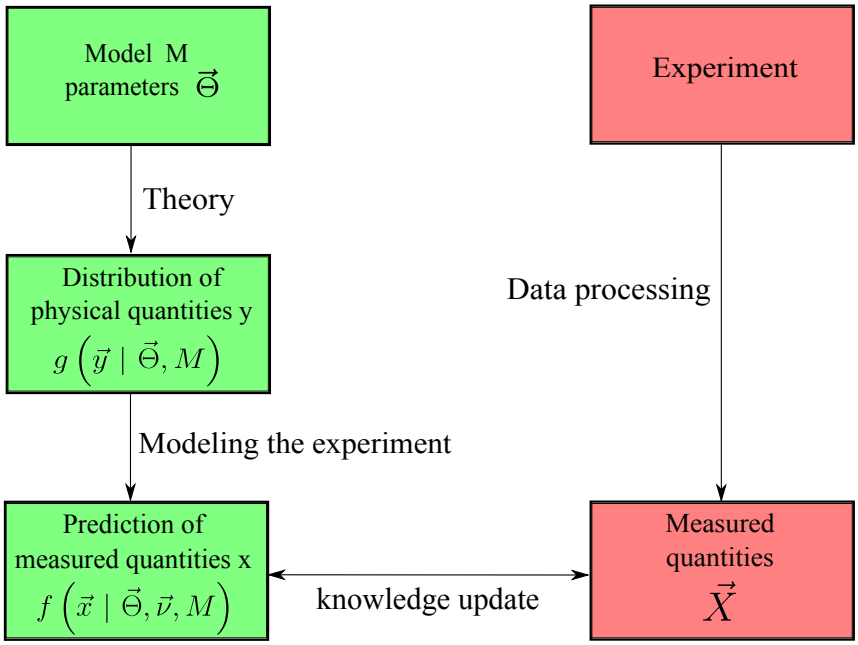

Figure 3.2.: The prediction of the measured quantities $\vec{x}$ are updated by gathering more data $\vec{X}$. During the modeling of the experiment usually nuisance parameters $\vec{\lambda}$ and extra assumptions are added in addition to the model parameters $\vec{\Theta}$. [13]

other analysis tools such as ROOT [3] and offers several output formats, from ASCII files to ROOT Trees and graphical displays. The implementation and formulation of the models is done in form of methods which belong to different predefined classes. For detailed information of the provided class structures and the methods see [14]. To determine the posterior pdf MCMC is used.

3.3.1 Markov Chain Monte Carlo

As mentioned above, for obtaining the posterior probability (3.10), which can be a complicated distribution in many dimensions, Markov Chain Monte Carlo is used. In BAT the Metropolis MCMC algorithm [19] is implemented. This algorithm does the following steps to map out a function $f(\vec{x})$:

1. At some random position $\vec{x}_i$ the chain starts.
2. For a symmetric pdf $g(\vec{x}_i, \vec{y})$ a point $\vec{y}$ is generated.
3. For both values, $\vec{x}_i$ and $\vec{y}$, the function is calculated and compared:
   - for $f(\vec{y}) \geq f(\vec{x}_i)$ set $\vec{x}_i = \vec{y}$
   - otherwise a random number of a flat distribution D_{flat} between [0,1] is generated and set $\vec{x}_{i+1} = \vec{y}$ if $f(\vec{y})/f(\vec{x}_i) > D_{flat}$, else set $\vec{x}_{i+1} = \vec{x}_i$.

4. Back to 1.

The limiting factor of this chain, for a reasonable function $g(\vec{x}, \vec{y})$, is the function $f(\vec{x})$. It is possible to randomly sample points (parameters of the model) according to complicated functions (pdfs) having an unknown, but somehow calculable, analytic form.

3.3.2 Implementation

One of the aims of BAT is to provide the user with an easy way for code implementation for a particular model. The model class `BCModel` provides the infrastructure and the links to individual algorithms and is parent to all user models.

Implementation is straightforward and is done by implementing an extended class which inherits from `BCModel`. To actually define a model the following steps are necessary:

1. Each parameter Θ_i has to be defined together with its range by calling the method:
   `int AddParameter(const char * name, double min, double max)`
2. Define the likelihood $\mathcal{P}(\vec{\Theta}|X)$ by implementing the method:
   `double LogLikelihood(std::vector<double> params)`
3. Define the prior $\pi(X)$ by implementing the method:
   `double LogAPrioriProbability(std::vector<double> params)`

To grant more numerical stability right from the beginning the natural logarithm of the probability is returned by the methods `LogLikelihood` and `LogAPrioriProbability`.

BAT can either be used in a ROOT interactive session (e.g. a macro) or can be used from a compiled program which is linked against the BAT libraries. It also provides a shell script to create a skeleton for a model class with a main program together with a makefile. The `CreateProject.sh` script was used to create the project for the Bayesian analysis done in section 5.2.

3.3.3 Output

BAT provides several standard output methods:

- Text files:
  When selected BAT creates a file with a summary for each model and its parameters. It contains the results of the analysis, e.g. mean and modes of the marginalized distributions, the level of information can be set by the user. In addition a log file for debugging is produced.
- ROOT files:
  Because ROOT is widely established as an analysis framework BAT also provides the possibility to write almost everything obtained in the analysis into a `.root` file. There is a huge functionality provided by the ROOT class `TFile` for storing

information. For each model a single file is produced with user defined content of information.

- Plot files:
  The drawings are also done using the ROOT functionality. Therefore every output format supported by ROOT can be chosen to save the plots. There is a predefined drawing style for 1-D and 2-D marginalized distributions to print them into a singe multi-page postscript file.

With the Bayesian inference introduced, the next chapter will focus on the PMT response. The response directly influences the measured differential energy rate spectra and so also has impact on the calculated CLs in the Bayesian analysis.

4 PMT response studies

To get a better understanding of the response from the PMTs and to check the model of Poisson distributed generation of photoelectrons, followed by a Gaussian distributed generation of photoelectrons inside the PMTs, this process is simulated and compared to the real response of the XENON100 PMTs [6] for a neutron calibration data set.

4.1 Description of the response

An incoming amount of photons N_γ, uniformly distributed, hitting a PMT generate $N_{p.e.}$ Poisson distributed photoelectrons. The probability of getting $N_{p.e.}$ instead of N_γ photoelectrons is then given by

$$P_{N_\gamma}(N_{p.e.}) = \frac{N_\gamma^{N_{p.e.}}}{N_{p.e.}!} \cdot \exp(-N_\gamma). \tag{4.1}$$

In the amplification process inside the PMT these N_{pe} photoelectrons become Gaussian distributed and form the measured signal S1:

$$f(S1|N_{p.e.}) = \frac{1}{\sqrt{2\pi\sigma^2}} \cdot \exp\left(\frac{(S1 - N_{p.e.})^2}{2\sigma^2}\right), \tag{4.2}$$

where $N_{p.e.}$ is the expectation value and σ^2 the variance ($\sigma = \sqrt{N_{p.e.}} \cdot \sigma_{PMT}$) of the Gaussian distribution, as shown in (2.14). In Fig. 4.1a histograms for different values of σ_{PMT} with an expectation value $< N_{p.e.} >= 0.8$ are shown. As one would expect, the higher σ_{PMT} gets the broader gets the distribution. The average single photoelectron response width $\sigma_{PMT} = 0.5$ has been measured in LED calibrations of the XENON100 detector [6]. The impact of different expectation values is shown in Fig. 4.1b. Since Poisson distributions only yield positive results, for small expectation values (e.g. the red distribution in 4.1a) a "tail" to the right and small bumps in the shape are visible that vanish for higher values.

4.2 Simulation of the response

A small program in `C++` is developed to simulate the behavior for different values of σ_{PMT} to see its impact (see B.1). To compare the simulated data with actual measurements, neutron calibration data of the XENON100 detector was used. There are several calibration measurements done for the XENON100 detector regularly. The calibration with neutrons is done with an AmBe source. With this source the reactions to nuclear recoils between the xenon nuclei and neutrons are studied to see what kind of signals such interactions produce. After the calibration some isotopes of the xenon

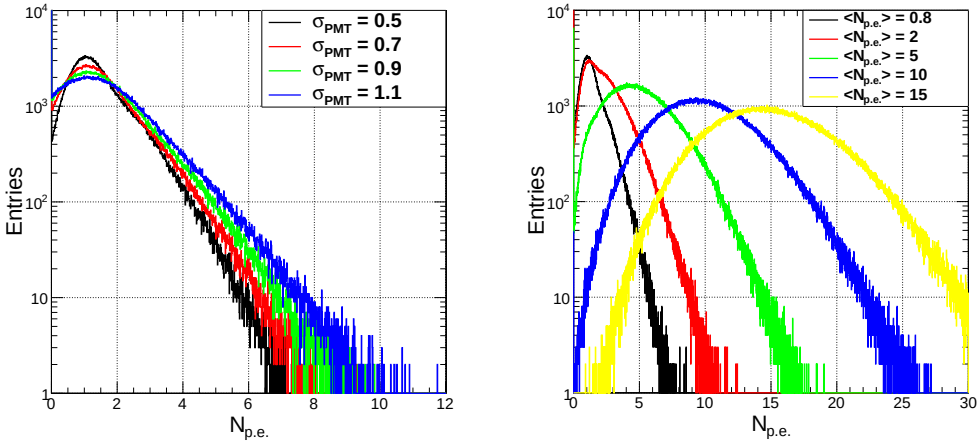

(a) PMT response simulations for different average SPE widths

(b) PMT response simulations for different expectation values

Figure 4.1.: PMT response simulations for expectation values and SPE widths

inside the TPC are in an excited metastable state from the interactions with the neutrons. They decay sending out characteristic emission lines at 164 keV for ^{131m}Xe and 236 keV (196 keV followed by a 40 keV disexcitation) for ^{129m}Xe. As disexcitation into its ground state takes place over approximately 8 or 11 days (depending on the isotope) the detector is illuminated uniformly. During this time all PMTs will get a light signal and the measurement is done [5]. Figure 4.2 shows the two lines in the cS2 vs. cS1 plane as the XENON100 detector detects them. The red ellipses in the 164 keV line (left population) indicates the 1σ, 2σ and 3σ region of the line. The second population represents the 236 keV line.

For analysis, the detector is divided into voxels [25] (a binned volume with 16 slices, each slice divided into 98 regions), see Fig. 4.3 for one slice and its 98 areas which follow the pattern of the top PMT array. The comparison is done with the 164 keV line. A histogram for each PMT (98 on the top and 80 on the bottom of the TPC) and voxel is created and filled with the photoelectrons detected. This leads to a total of 279104 histograms for the data file. Every PMT sees a different amount of light, depending on its position and which voxel is observed, leading to different amount of entries in the histograms. To make this more comparable, and to reduce the amount of data, only the mean value and the Root Mean Square (RMS) of the histograms (for simulation and data) are taken into account. There is also a selection of empty histograms (where PMTs did not detect any light) or noisy PMTs in the data file.

Figure 4.4a shows a 2D histogram where every point represents one histogram with its corresponding mean value and RMS. In the Simulation, for each generated value of photons (uniform distributed between 0 and 20) a histogram is filled with the modeled response, see (4.1) and (4.2). This is repeated 100 times to get more statistics. In the

first simulation the default value for $\sigma_{PMT} = 0.5$ was used.

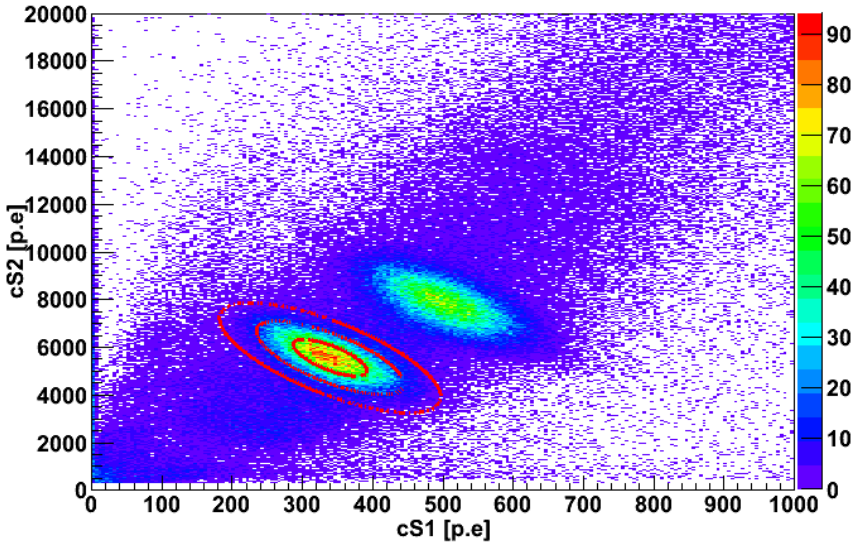

Figure 4.2.: To visualize the event selection the measurement with activated LXe is shown. The characteristic lines at 164 keV for ^{131m}Xe and 236 keV (40 keV + 196 keV) for ^{129m}Xe are visible [17].

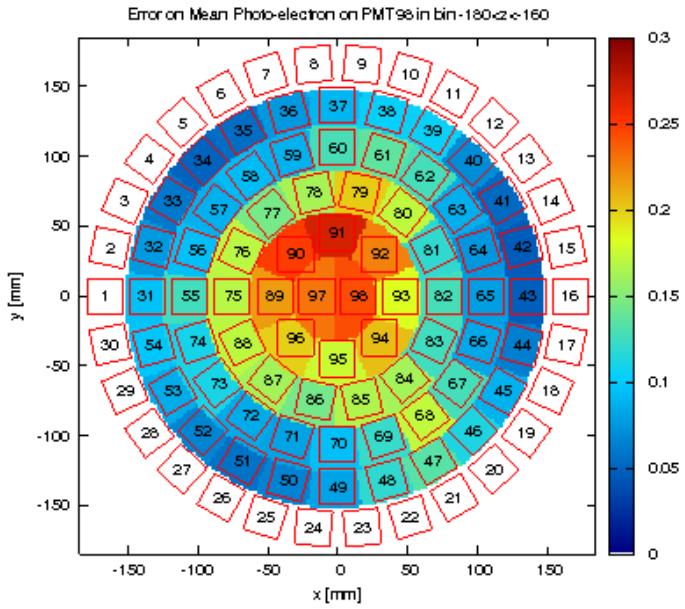

Figure 4.3.: Slice with areas for the volume binning (voxels) of the XENON100 detector. The color scale is not from interest and can be ignored. [25]

The discrepancy, shown in Fig. 4.4a, between data and simulation with default $\sigma_{PMT} = 0.5$ is clearly visible. To make the differences more visible and comparable a profile of the 2-D histogram is done, see Fig. 4.4b. The same simulation was also done with $\sigma_{PMT} = 0.7$ (see Fig. 4.5a), $\sigma_{PMT} = 0.9$ (see Fig. 4.6a) and $\sigma_{PMT} = 1.1$ (see Fig. 4.7a). For $\sigma_{PMT} = 0.7$ the simulation still lies below the data and for $\sigma_{PMT} = 1.1$ the simulation already is above most of the data. Out of the three values $\sigma_{PMT} = 0.9$ was the best fitting one in the range of 0 to 10 p.e. $S1_i$ mean value ($i = 1, \ldots, 178$ for the 178 PMTs). Why there was a different value measured for σ_{PMT} through LED calibrations with the SPE spectrum has to be further investigated. Since the average response was obtained with SPE spectra, calibrations with more light are planed in the future. Also the model for the PMT response, see (2.14), may be assumed too simple and has to be modified with more complex algorithms.

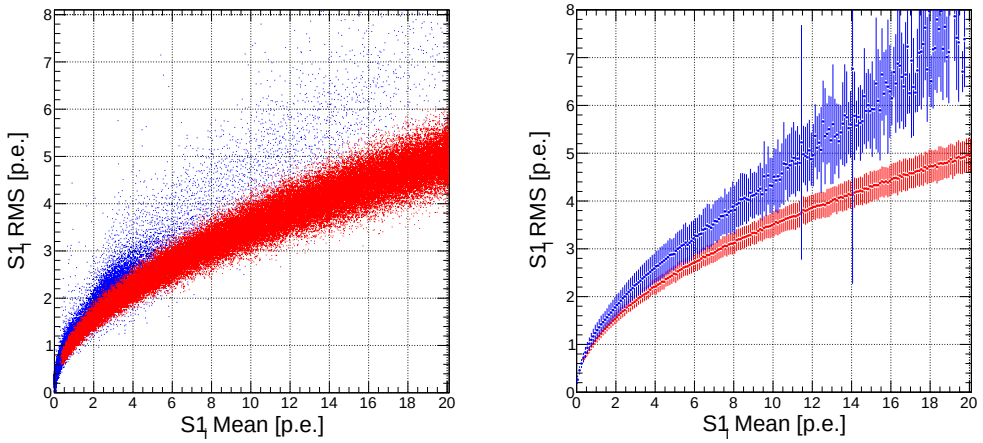

(a) 2-D histogram for mean value and RMS of data (blue) and simulation (red).

(b) Profile of data (blue) and simulation (red).

Figure 4.4.: Histogram (a) and profile (b) for data (blue) and simulation (red) with $\sigma_{PMT} = 0.5$. In the profile on the right, the discrepancy between simulation and data is clearly visible.

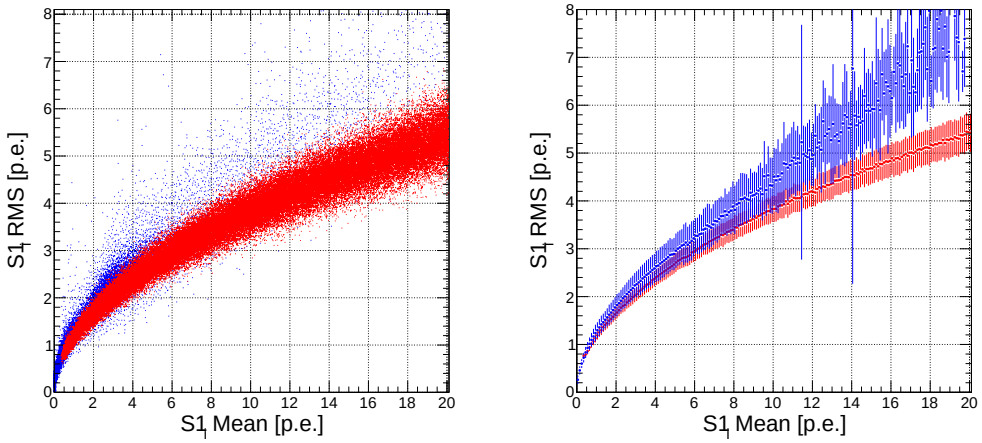

(a) 2-D histogram for mean value and RMS of data (blue) and simulation (red).

(b) Profile of data (blue) and simulation (red).

Figure 4.5.: Histogram (a) and profile (b) for data (blue) and simulation (red) with $\sigma_{PMT} = 0.7$. There is still a discrepancy between data and simulation in the profile (right) visible.

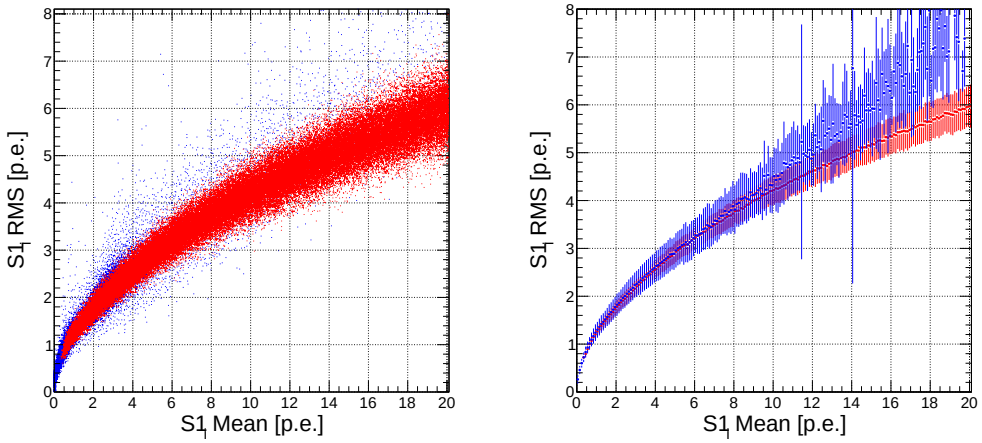

(a) 2-D histogram for mean value and RMS of data (blue) and simulation (red).

(b) Profile of data (blue) and simulation (red).

Figure 4.6.: Histogram and profile for data (blue) and simulation (red) with $\sigma_{PMT} = 0.9$. In the range from 0 to 10 $S1$ mean, the simulation seems to fits the observed data in the profile (right).

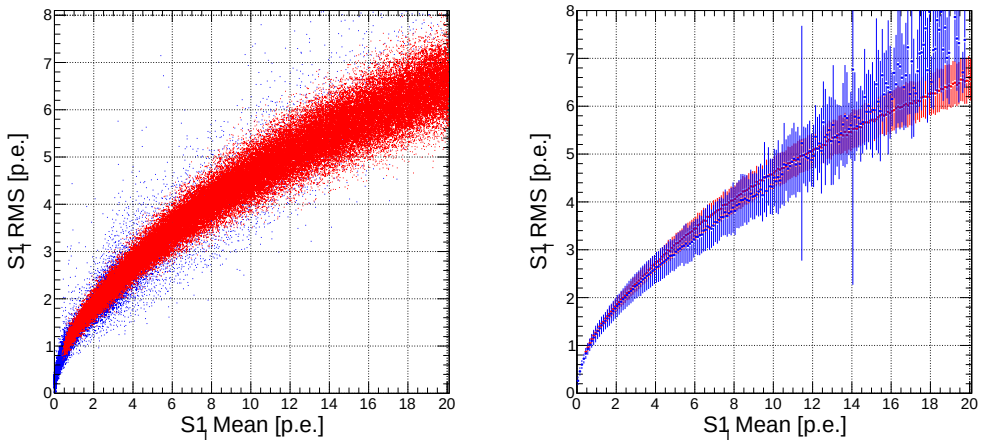

(a) 2-D histogram for mean value and RMS of data (blue) and simulation (red).

(b) Profile of data (blue) and simulation (red).

Figure 4.7.: Histogram and profile for data (blue) and simulation (red) with $\sigma_{PMT} = 1.1$. The simulation in the profile (right) starts to lay above the data, σ_{PMT} was chosen to high.

The deeper knowledge of the response of the PMTs is from big interest since the response directly influences the signal and therefore also the likelihood function used in the Bayesian analysis. To see the impact of a different SPE response width on the Confidence Limit for WIMP exclusion, in section 5.3.1 a calculation for $\sigma_{PMT} = 0.9$ will be done after confirming a reasonable result with the maximum gap method and default SPE response width $\sigma_{PMT} = 0.5$.

5 Dark Matter exclusion limits

Since WIMPs have not been discovered yet, only upper Confidence Limits (CLs) can be calculated for the cross-section of WIMP-nucleus interactions. A 90% CL for example implies that for a probability of 90%, no events can be observed above a certain cross-section. Two different methods, the maximum gap method [33] and a Bayesian approach, for limit calculations are studied. The maximum gap method was coded in `C++` to check the results of the scatter rate calculations $\mathrm{d}R/\mathrm{d}S1$. After confirming a reasonable result with the maximum gap method for XENON100 data finally the Bayesian limit analysis is done. All calculations will be done with respect to the last science run detector parameters (see [7]): an exposure of 224.5 days and fiducial volume of 34 kg LXe will be used. The exposure has to be considered in the calculations of the differential energy rates since they are calculated in units of events/kg/day/keV. Since the atomic number A has an impact on the calculated recoil energy rates, it should be noted that the in this work average isotope mass for xenon ($A = 131.29$) was used. For notation simplicity instead of the corrected values $cS1$ and $cS2$, $S1$ and $S2$ will be used if not explicitly mentioned otherwise.

5.1 Maximum gap method for limit setting

To test the developed code which follows the calculations done in section 1.3 and 2.3, the maximum gap method described in [33] is used. This method applies to small but unknown background together with known expected signal shapes. It does not depend on the binning of the data, is robust to cuts on the parameter range and provides true, but conservative classical one sided CLs.

If the background is completely known it would already be included in the expected spectrum of a measurement. Now assume an additional unknown background deteriorating the data. The aim for setting an upper CL is to change the cross-section σ in the calculations, see (2.21), of the differential event rate $\mathrm{d}R/\mathrm{d}S1$ until it will be rejected as too high. At first, a criterion for deciding when a signal gets to high is needed. To find the strongest (lowest) possible upper limit the region where a high signal is expected and the background is low has to be located. In the maximum gap method the biggest gap between two observed events (like the name of the method suggests) in the data set is the region of interest. Here the background should be low because nothing has been measured in between the two events, see Fig. 5.1 for example.

To apply this method, the first task is to find the maximum gap, which is the largest of the gaps between two measured events. In the XENON100 225 live days data, two events were observed in the benchmark region after data selection [7]. One event was observed at 7.1 keV, the other at 7.8 keV. In this case the maximum gap is quite obvious

and lies between the second event and the upper threshold. For example, Fig. 5.1 shows the spectrum of a 50 GeV WIMP with a reference cross-section of $\sigma_{ref} = 10^{-45}\,\mathrm{cm}^2$ calculated as described in (2.20). The whole energy window in which the XENON100 detector is sensitive and searches for WIMPs goes from 6.6 keV (3 p.e.) to 43.3 keV (30 p.e.), for conversion of E_{nr} to p.e. see (2.13).

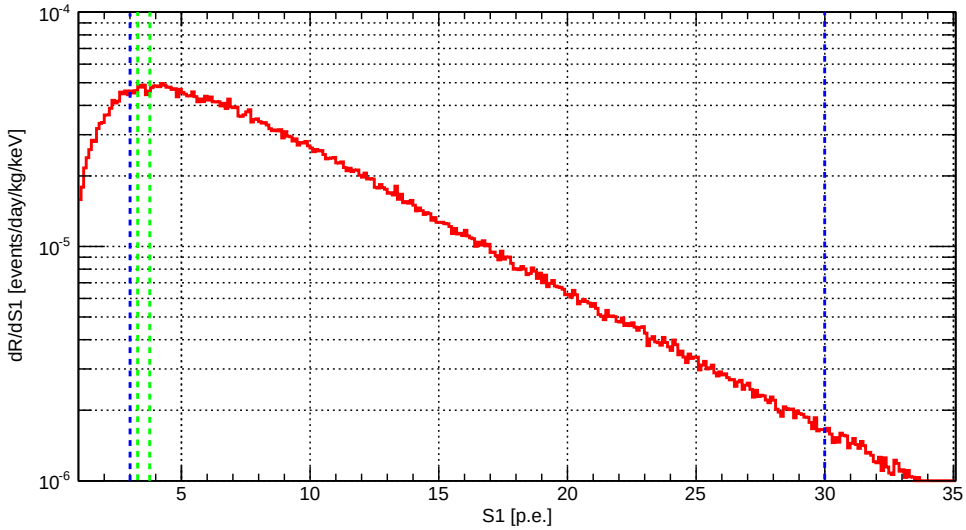

Figure 5.1.: Differential recoil energy spectrum for a 50 GeV WIMP. The blue (dashed) lines indicate the whole energy range from 6.6 keV (3 p.e.) to 43.3 keV (30 p.e.), the green (dashed) lines the two events in the benchmark region 225 live days, the lower at 7.1 keV (3.29 p.e.) and the second at 7.8 keV (3.76 p.e.).

The number of the expected events x in this gap is then defined through the integral of the known spectrum of the differential event rate $\mathrm{d}R/\mathrm{d}S1$:

$$x = \int_{E_{low}}^{E_{high}} \frac{\mathrm{d}R}{\mathrm{d}S1}\mathrm{d}S1, \tag{5.1}$$

where $E_{low} = 7.1\,\mathrm{keV}$ and $E_{high} = 43.3\,\mathrm{keV}$. With growing cross-section σ the size of the calculated rates in the maximum gap also grows. Let μ be the total number of events in the entire range of interest given by the detector thresholds from $E_{min} = 6.6\,\mathrm{keV}$ to $E_{max} = 43.3\,\mathrm{keV}$:

$$\mu = \int_{E_{min}}^{E_{max}} \frac{\mathrm{d}R}{\mathrm{d}S1}\mathrm{d}S1. \tag{5.2}$$

The CL at which large x excludes a signal is given by the equation

$$C_0(x,\mu) = \sum_{k=0}^{m} \frac{(kx-\mu)^k \mathrm{e}^{-kx}}{k!}\left(1 + \frac{k}{\mu - kx}\right), \tag{5.3}$$

where $m \leq \mu/x$ is the greatest integer smaller or equal to the fraction of μ divided by x. For the derivation of (5.3) see [33]. For a 90 % CL, the cross-section is increased until $C_0 \geq 0.9$. See appendix B.2 for the realization of this algorithm in the code.

To get the expected events in the maximum gap (x) and the whole energy window (μ) the differential rate is integrated between the corresponding boundaries. To find the 90 % CL a loop is programmed where the cross-section in the calculation of the differential rates is modified, and therefore the expected events obtained through the integration. The loop runs to the point where $C_0 \geq 0.9$, which causes the loop to break. The found cross-section, together with the corresponding WIMP mass, is filled into a graph. This is done for a given array of WIMP masses that cover the range from 6 to 1000 Gev/c^2. Finally the WIMP exclusion limit is obtained, see Fig. 5.2 and table A.1 for the corresponding cross sections.

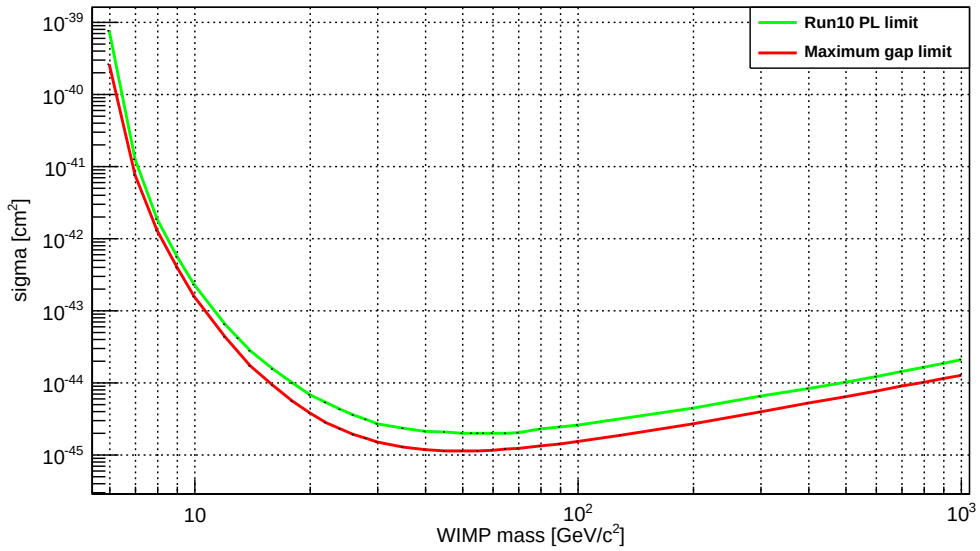

Figure 5.2.: The obtained maximum gap exclusion limit (red line) and the PL limit from 225 live days data (green line).

Since in this analysis uncertainties were not considered, the maximum gap method calculations yield more constraining limits as the 225 live days PL limit [7]. In general as a check for the event rate calculation the result is satisfying enough to go on to the Bayesian inference.

5.2 Bayesian limit

For this analysis, several parameters have to be defined first. The likelihood function is chosen according to the profile likelihood analysis, see [4] for reference. To be able to compare the outcome of the Bayesian calculations to the 225 live days limit all detector parameters and the data sets are chosen accordingly. As the PL method only considers flat prior distributions for the parameters of interest, the prior pdf was also chosen to be flat in the Bayesian approach at first.

In Bayesian inference the prior is not constrained to be flat like in the PL method. If prior knowledge yields a certain shape for the pdf of a parameter it can be chosen accordingly.

5.2.1 Data set

The data is usually plotted in a 2D histogram with $S1$ in the x-axis and $(\log(S2/S1) - \log(S2/S1)_{\mathrm{ER_{mean}}})$ on the y-axis, called flattened space. This representation is chosen because within one $S1$ bin, the variation of $\log(S2/S1)$ is small enough to be described by a mean value $(\log(S2/S1)_{\mathrm{ER_{mean}}})$ and therefore flattened. With the help of AmBe calibration measurements, see Fig. 5.3, the data-space is divided into 12 bands. For each bin in $S1$ (the x-axis) the events are equally shared between the 12 bands on the y-axis, to have the same statistics within each band [6]. Each event, nuclear (signal) or electronic recoil (background), has now an associated probability to fall into a certain band. The calibration measurements are done to know how the detector responds to electronic and nuclear recoils. Three different sets of data are needed for the analysis:

Nuclear recoil calibration data

To estimate how the detector responds to nuclear recoils, a calibration with neutrons from an AmBe source is done before and after the science runs. The bands are defined using this data (see Fig. 5.3).

Background calibration data

To be able to better characterize background events from electronic recoils a calibration with β and γ radiation (^{60}Co) is done twice a week (see Fig. 5.4). It is also used for energy calibration of the detector and therefore done more often as the calibration for nuclear recoils.

Science data

Between the calibration and background measurements, the actual DM measurements are done, when no radioactive source is near the detector (science data, see Fig. 5.5).

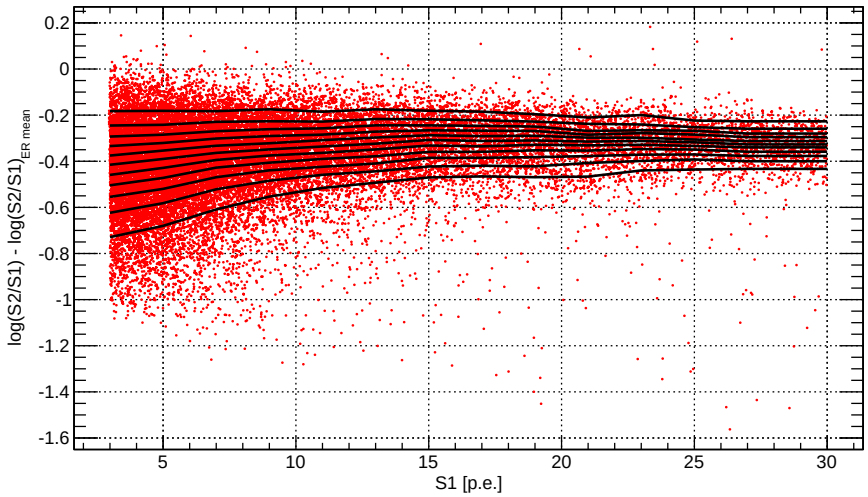

Figure 5.3.: AmBe 225 live days nuclear recoil data (red dots) with the 12 bands (black lines). By construction, the events are equally shared between the 12 bands.

This data set is blinded to avoid biased assumptions before a whole data set is complete. Only calibration data is used to develop cuts and acceptances.

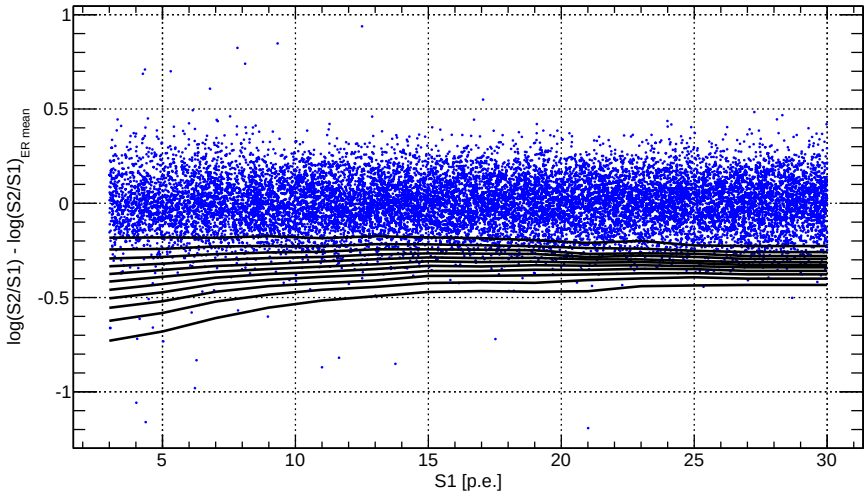

Figure 5.4.: ^{60}Co 225 live days electronic recoil data (blue dots) with the 12 bands (black lines). Electronic recoils are the main part of the expected background events in the science data.

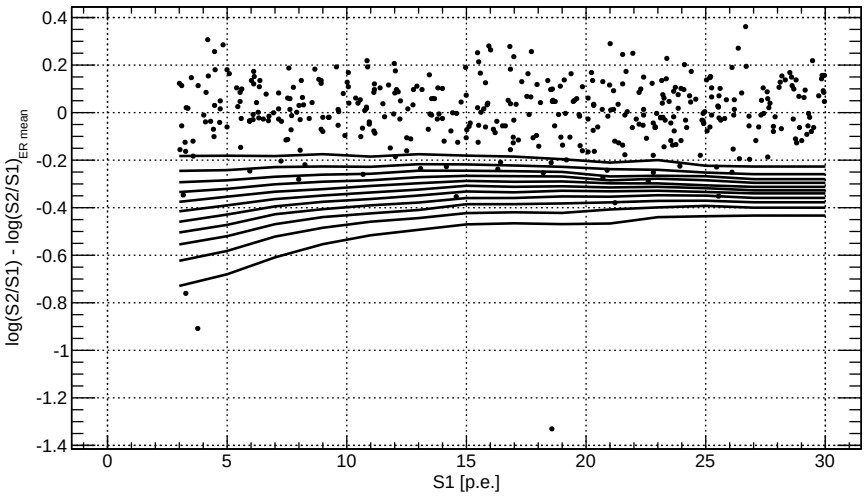

Figure 5.5.: DM science data for 225 live days (black dots) with the 12 bands (black lines) after data selection.

Basic cuts on the science data

The cuts derived from the calibration measurements, which are applied to the science data set are e.g.:

- Basic quality cuts: Remove events that show an excessive level of noise or light.
- Selection of single-scatter events: WIMPs are expected to interact only once inside the TPC.
- Selection of the fiducial volume: Removes noisy areas with high number of background events (outer part of the TPC volume).
- Energy selection and threshold cut on $S2$: Only accept events that are above a certain energy threshold.

For more and detailed information on the cuts, see [6].

5.2.2 Calculation of the S1-spectrum

The following calculations are needed for the later implementation into the analysis tool. They mainly follow the calculations done in in previous sections (see (2.14)), for reference see also [6].

With the relative scintillation yield of nuclear recoils $\mathcal{L}_{\text{eff}}$ (see Fig. 2.6 or 2.7) the expected number of photoelectrons for a given recoil energy E_{nr} can be calculated (see

also (2.13)):

$$cs1(E_{nr}) = E_{nr}\langle L_y\rangle \mathcal{L}_{eff}\frac{S_{nr}}{S_{ee}}, \tag{5.4}$$

where $S_{nr} = 0.95$ and $S_{ee} = 0.58$ are the quenching factors depending on the applied electrical field in the TPC for nuclear (nr) and electronic (ee) recoils and $L_y(122\,\mathrm{keV}_{ee}) = 2.28\,\mathrm{PE/keV}_{ee}$ is the normalized light yield. Because these factors have been measured very well the corresponding errors are small and are neglected for the analysis [4].

Following (2.20) the signal rate in events per number of photoelectrons N_{pe} is calculated:

$$\frac{\mathrm{d}R}{\mathrm{d}N_{pe}} = \int \frac{\mathrm{d}R}{\mathrm{d}E_{nr}}(E_{nr}; m_\chi)\,\mathrm{Poi}(N_{pe}|s1(E_{nr}))\,\epsilon_2(E_{nr})\,\mathrm{d}E_{nr}. \tag{5.5}$$

Considering also the finite average single-photoelectron resolution of the XENON100 PMTs we get the S1-spectrum (analogously to (2.20)):

$$\begin{aligned}\frac{\mathrm{d}R}{\mathrm{d}S1} &= \epsilon_1(S1)\sum_{N_{pe}} p_{pmt}(S1|N_{pe}, \sqrt{N_{pe}}\cdot\sigma_{PMT})\,\frac{\mathrm{d}R}{\mathrm{d}N_{pe}} \\ &= \epsilon_1(S1)\int \frac{\mathrm{d}R}{\mathrm{d}E_{nr}}\epsilon_2(E_{nr})p_{S1}(S1|E_{nr})\mathrm{d}E_{nr}.\end{aligned} \tag{5.6}$$

Where $p_{S1}(S1|E_{nr})$ is defined as in (2.15). The total amount of expected signal events N_s is calculated solving the integral:

$$N_s(\sigma) = \int_{S1_{min}}^{S1_{max}} \frac{\mathrm{d}R}{\mathrm{d}S1}(m_\chi)\mathrm{d}S1, \tag{5.7}$$

where the integral boundaries $S1_{min} = 3\,\mathrm{p.e.}$ and $S1_{max} = 30\,\mathrm{p.e.}$ represent the energy interval considered in the analysis. The spectral shape of the normalized WIMP spectrum $f_s(S1; m_\chi)$ is given by

$$f_s(S1; m_\chi) = \frac{\frac{\mathrm{d}R}{\mathrm{d}S1}(m_\chi)}{\int_{S1_{min}}^{S1_{max}} \frac{\mathrm{d}R}{\mathrm{d}S1}(m_\chi)\mathrm{d}S1}. \tag{5.8}$$

N_s only carries the information about the amount of expected events, the information about the shape is manifested completely in the normalized spectrum f_s.

5.2.3 Construction of the likelihood function

The construction of the likelihood function follows [4]. The first term contains the information from the signal expected in the XENON100 detector and describes the

main measurement. The likelihood that a set of n_j data points in band j emerges from a given WIMP spectrum is given by

$$\mathcal{L}_1 = \prod_{j=1}^{k} \mathrm{Poi}(n_j|\epsilon_s^j N_s + \epsilon_b^j N_b) \prod_{i=1}^{n_j} \frac{\epsilon_s^j N_s f_s(x_i) + \epsilon_b^j N_b f_b(x_i)}{\epsilon_s^j N_s + \epsilon_b^j N_b}, \tag{5.9}$$

where

- k : amount of bands considered
- ϵ_s^j : probability for signal event to fall in band j
- ϵ_b^j : probability for background event to fall in band j
- N_s : expected signal events $N_s(m_d, \sigma)$, see (5.7)
- N_b : expected background events
- M_s : number of nuclear recoil calibration events
- M_b : number of electronic recoil calibration events
- m_j^s : number of signal events in band j
- m_j^b : number of background events in band j
- n_j : data points in band j
- f_s : normalized WIMP spectrum, see (5.8)

By construction, all ϵ_s^j should have the same value equal to 1/12, when 12 bands are modeled. As can be seen in the background data, see Fig. 5.4, ϵ_b^j should decrease with rising band number. In the last few bands almost no background events from electronic recoils are expected.

The purpose of the following terms is to constrain the nuisance parameters ϵ_s^j and ϵ_b^j in the main likelihood function $\mathcal{L}_1$, their precision depends on the amount of measured calibration data:

$$\mathcal{L}_2 = \prod_{j=1}^{K} \mathrm{Poi}(m_s^j|\epsilon_s^j M_s), \tag{5.10}$$

$$\mathcal{L}_3 = \prod_{j=1}^{K} \mathrm{Poi}(m_b^j|\epsilon_b^j M_b). \tag{5.11}$$

The whole likelihood function considered for the Bayesian analysis is then given by:

$$\begin{aligned}\mathcal{L} = &\prod_{j=1}^{K} \mathrm{Poi}(n_j|\epsilon_s^j N_s + \epsilon_b^j N_b) \prod_{i=1}^{n_j} \frac{\epsilon_s^j N_s f_s(x_i) + \epsilon_b^j N_b f_b(x_i)}{\epsilon_s^j N_s + \epsilon_b^j N_b} \\ &\times \mathrm{Poi}(m_j^b|\epsilon_b^j M_b) \times \mathrm{Poi}(m_j^s|\epsilon_s^j M_s)\end{aligned} \tag{5.12}$$

To be able to mathematically handle this equation better we apply the natural logarithm and get the log-likelihood function:

$$\log\mathcal{L} = \sum_{j=1}^{K}\left(\sum_{i=1}^{n_j}\log(\epsilon_s^j N_s f_s(x_i) + \epsilon_b^j N_b f_b(x_i)) + m_j^b \log(\epsilon_b^j M_b) + m_j^s \log(\epsilon_s^j M_s)\right) - N_s - N_b - M_s - M_b \tag{5.13}$$

This is the needed form of the likelihood function for implementation in BAT. The spectral shape of the background distribution is assumed to be flat [4]. The expected amount of background events N_b in the range of 3-30 p.e. is estimated to be 412. For more information on the background model see [23]. At first we only assume the cross-section to be a parameter, with a flat (in log space) prior distribution. Only the parameter range will have prior knowledge in form of the upper boundary of the old XENON10 detector (predecessor to the XENON100 detector) WIMP exclusion limit, multiplied by a factor of two. The factor was introduced to reduce the weight of this biased assumption. The lower boundary of the parameter range will be flat and is set way below the best known limit of the XENON100 PL analysis to $1 \cdot 10^{-46}\,\mathrm{cm}^2$. No nuisance parameters are introduced in the beginning, the probabilities of ϵ_s^j and ϵ_b^j are calculated directly from the ratio of m_j^s/M_s and m_j^b/M_b. The amount of expected background events N_b will be a constant. The uncertainty of $\mathcal{L}_{\mathrm{eff}}$ is also not implemented.

5.2.4 Implementation into the Bayesian Analysis Toolkit

With the `CreateProject.sh` script provided by BAT the project `xsec` is created. Four files are automatically produced:

- `xsec.h`: Header file, contains forward declarations of variables, classes and functions that are available to other files by including the header (e.g. in the `xsec.cxx` and `runxsec.cxx` file).

- `xsec.cxx`: `C++` file that includes the definitions and input parameters with classes that have to be overloaded. The biggest part of the work is done here e.g. implementation of the likelihood function, looping over the data files.

- `runxsec.cxx`: Contains the main function where everything is put together. All needed instances of the classes are created, the MCMC calculation can be tuned and also the output is defined.

- `Makefile`: File to compile the code and create the executable to run the analysis.

For the input, each data file (science data, AmBe calibration, ^{60}Co calibration (background)) is stored in form of a `.root` file which contains 12 `TGraph` objects (graphs saved with ROOT's `TGraph` class) according to the 12 defined bands. To access the data points stored in e.g. band 4 the fourth graph in each file has to be called. By dividing the data before analysis, there is no need to recalculate the bands every time, which saves a lot of time during the later iterations in the MCMC sampling.

The file that holds the most information and also needs the most input is the `xsec.cxx` file, see appendix B.3 for a snippet of the code. The output format was chosen to directly produce plots and text files with the results. Also, all calculated parameters were saved as a `.root` file so they can be accessed for further processing. A loop over an array of masses is done like before in the maximum gap method. For each mass the output files are created separately, all MCMC chains run for 100000 iterations.

5.3 Results of the first Bayesian Calculations

To be able to compare the Bayesian results to the PL method, the same quantiles are also used in the Bayesian analysis. They can be accessed through the produced `.root` files. In Fig. 5.6, 5.7 and 5.8 three examples (a low mass of 6 GeV, a medium mass of 50 GeV and a high mass of 1000 GeV) for the resulting probability density functions are shown. The red vertical lines mark the 90 % quantile of the pdfs.

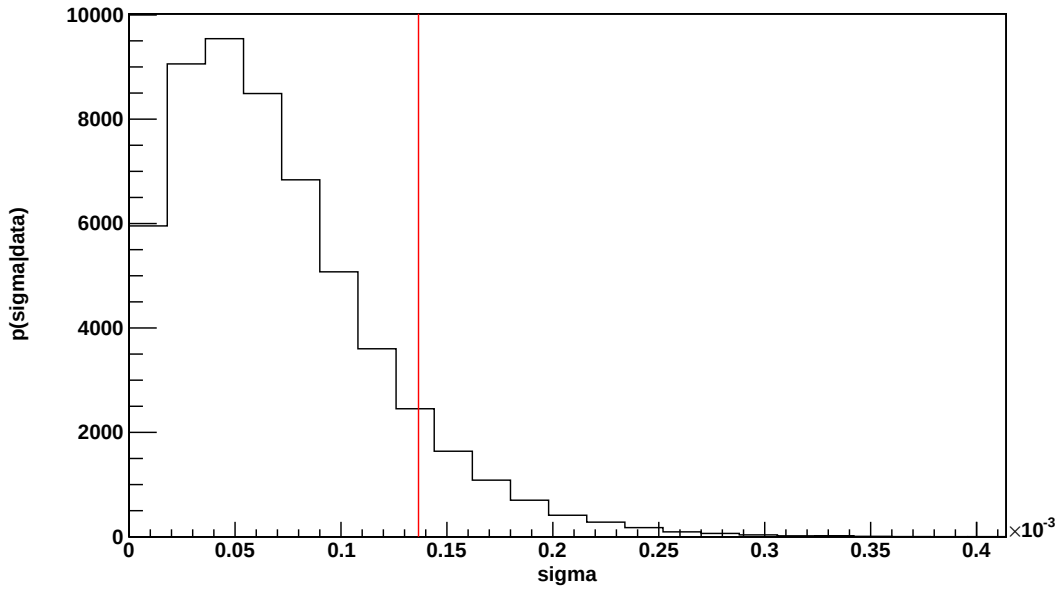

Figure 5.6.: Probability density function for a 6 GeV WIMP for the Bayesian calculations done with BAT. The red vertical line marks the 90 % quantile at a cross-section of $\sigma = 1.37 \cdot 10^{-40}\,\mathrm{cm}^2$.

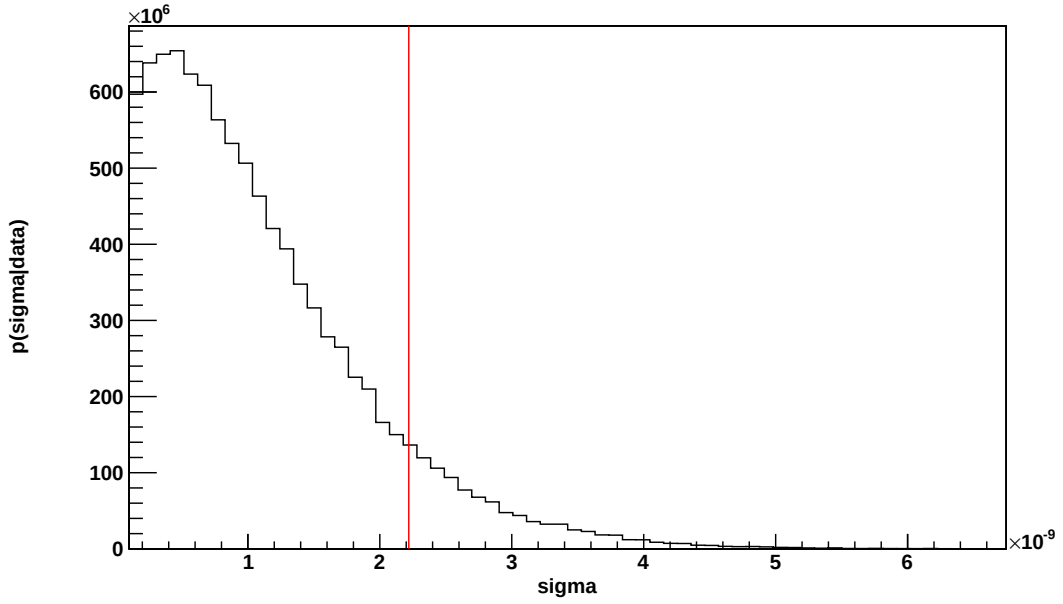

Figure 5.7.: Probability density function for a 50 GeV WIMP for the Bayesian calculations done with BAT. The red vertical line marks the 90 % quantile at a cross-section of $\sigma = 2.22 \cdot 10^{-45}\,\mathrm{cm}^2$.

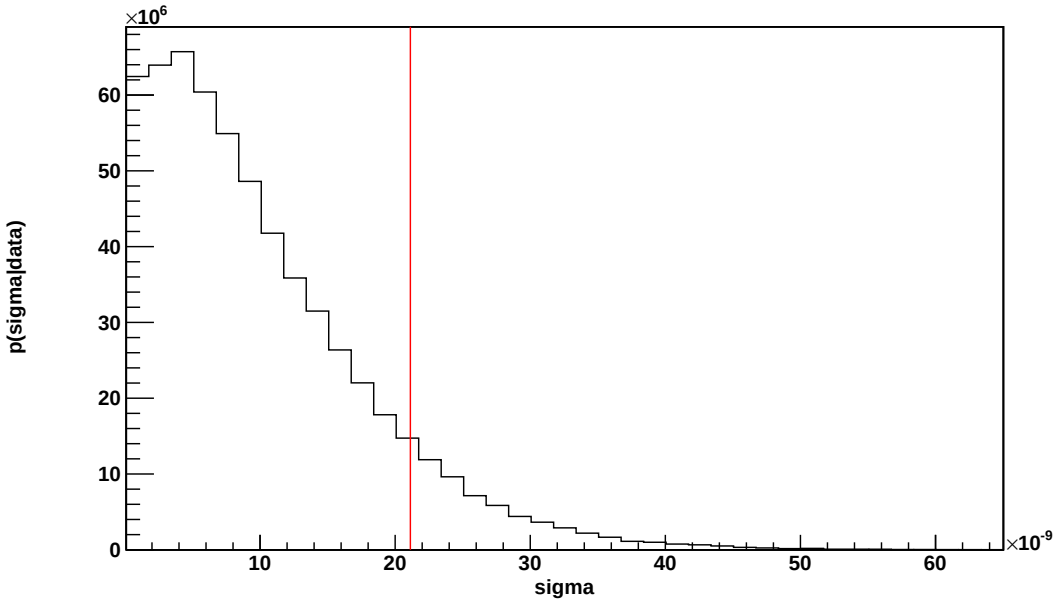

Figure 5.8.: Probability density function for a 1000 GeV WIMP for the Bayesian calculations done with BAT. The red vertical line marks the 90 % quantile at a cross-section of $\sigma = 2.11 \cdot 10^{-44}\,\mathrm{cm}^2$.

In table A.2 all 90 % quantiles with their corresponding WIMP masses are shown. Finally in Fig. 5.9 the calculated exclusion limit with Bayesian reasoning is plotted (red line). For comparison the plot includes the limit from the 225 live days PL analysis (green line). Also the used parameter range for the sampled cross-section (black and blue dashed lines) is visible.

The Bayesian limit is more constraining than the limit obtained with the PL method for lower masses. For masses above 20 GeV the limit is less constrining but the differences are very small. Figure 5.10 shows the difference between the Bayesian and the PL limit. Since there are no uncertainties implemented in the Bayesian calculations, the rising difference of the limits towards lower WIMP masses is not surprising but needs further investigation. For small recoil energies, produced by a WIMP-nucleus interaction, the uncertainties play a bigger role which translate into a bigger difference in the limit. With the future implementation of uncertainties on e.g. the relative scintillation yield of nuclear recoils $\mathcal{L}_{eff}$ and other nuisance parameters the limit is supposed to get less constraining. In section 5.3.2 a first attempt to define a nuisance parameter will be done. Instead of a constant amount of background events $N_b = 412$ p.e. an unknown amount will be considered.

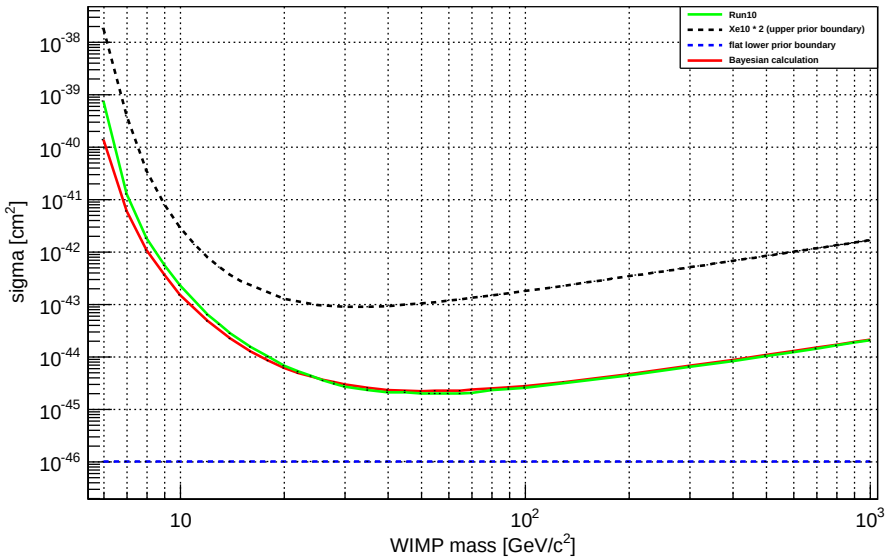

Figure 5.9.: Bayesian WIMP exclusion limit (red line) compared to the 225 live days PL limit (green line) together with the upper (black dashed line) and lower (blue dashed line) parameter boundary.

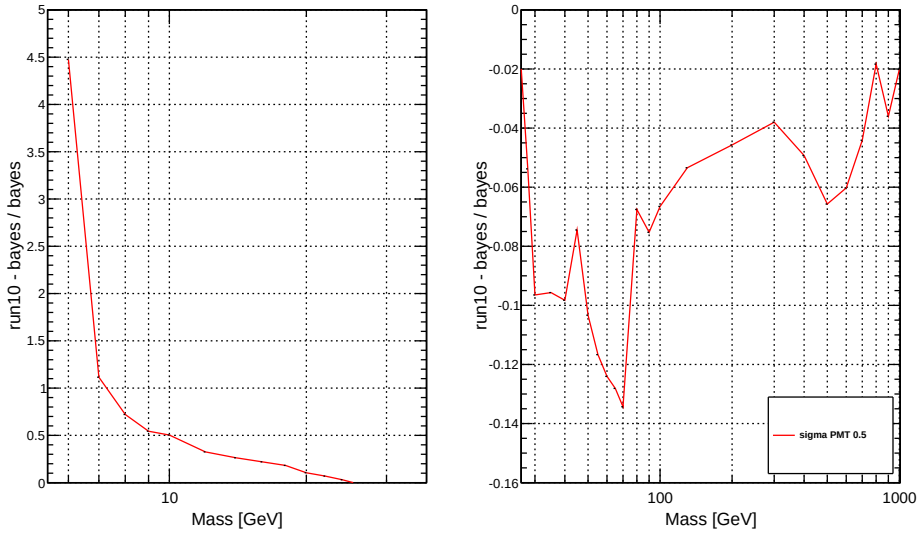

Figure 5.10.: Comparison of the Bayesian and PL 225 live days limit. An increasing discrepancy towards lower WIMP masses, due to the bigger impact of uncertainties on low recoil energies, is observed.

5.3.1 Results with different single photoelectron response width

To see the impact of a different choice for the single photoelectron (SPE) response width, a calculation with $\sigma_{PMT} = 0.9$ is done. Since for a broader differential energy rate spectrum (see Fig. 4.1a) more upward fluctuations above the energy threshold are possible for low recoil energies, the limit will get more constraining in these regions. For higher WIMP masses there should be only a small effect and the limit should get less constraining because the differential energy rates get slightly smaller when they get broader, resulting in a overall loss in the differential energy rate. Figure 5.11 shows the outcome with modified σ_{PMT} calculations and Fig. 5.12 shows again the difference with respect to the PL limit.

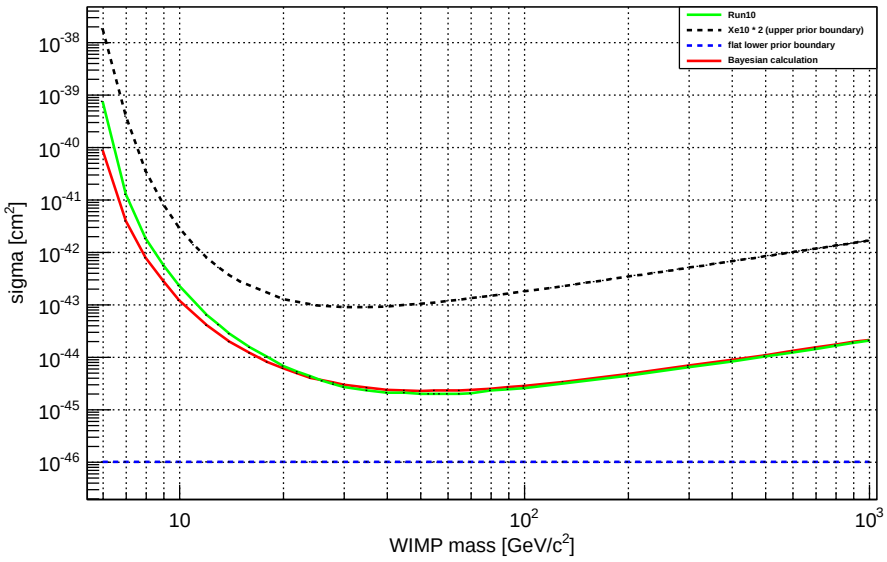

Figure 5.11.: Bayesian WIMP exclusion limit for the choice of $\sigma_{PMT} = 0.9$ (red line) compared to the 225 live days PL limit (green line) together with the upper (black dashed line) and lower (blue dashed line) parameter boundary.

As already guessed, the limit gets more constraining for low WIMP masses as more events fluctuate over the energy threshold of the detector. Above 30 GeV on the other hand, the limit gets less constraining. Obviously it will be an important task for the future to estimate the right SPE response width or find an improved model to better describe it. For bigger values of σ_{PMT} a change of the exclusion limit in the favor of small mass WIMPs can be concluded.

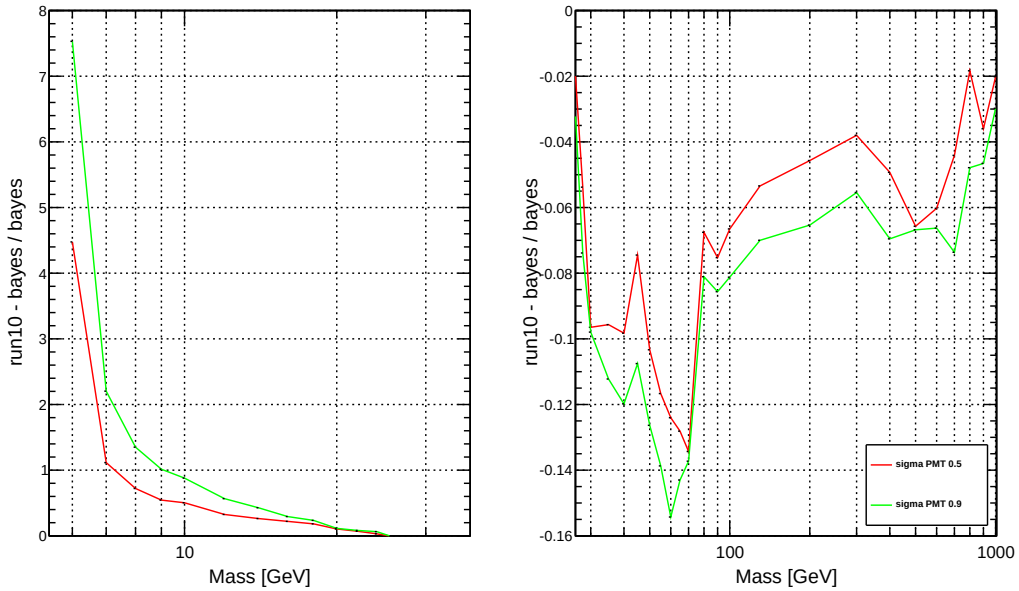

Figure 5.12.: Comparison of the Bayesian (blue line) and PL 225 live days limit for $\sigma_{PMT} = 0.9$. For direct comparison also the difference of the limit for $\sigma_{PMT} = 0.5$ (red line) is included.

5.3.2 Results with N_b as a nuisance parameter

To get a hold on the influence of N_b as a nuisance parameter, an additional calculation is done. In Bayesian inference the nuisance parameters are treated as described in section 3.2.2. During the MCMC sampling the additional parameter, in this case N_b, is integrated out by introducing it as an additional free parameter but afterwards flagging it as a nuisance parameter. In BAT, this is done with: `GetParameter(`N_b`)->SetNuisance(1)`. Figure 5.13 shows the corresponding limit and Fig. 5.14 again shows the comparison with respect to the 225 live days PL limit.

The comparison shows, that with a nuisance parameter included in the calculation, the limit is mostly closer to the 225 live days PL limit, or at least the difference is the same. In general it can be assumed, that the introduction of nuisance parameters makes the limit less constraining because there is more freedom in the sampling. N_b is sampled for each mass, since the program (at least for now) is not able to share parameters between the runs. In Fig. 5.15 the resulting N_b for each mass is shown. Instead of 412 events as estimated in the background model [23] the calculations yield lower values in a constant range of 397 to 398 events, which is less than 5 % difference. Even if N_b is sampled independently for every mass the parameter stays constant.

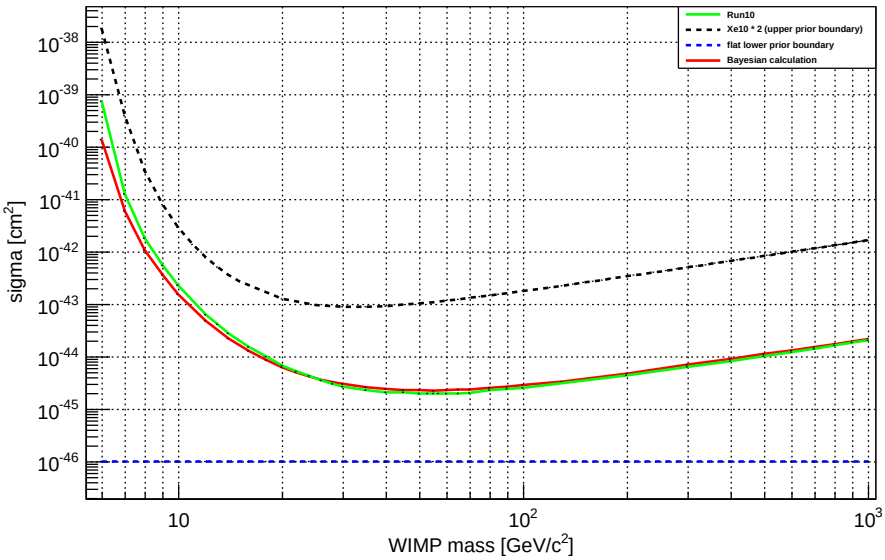

Figure 5.13.: Bayesian WIMP exclusion limit with N_b as nuisance parameter (red line) compared to the 225 live days PL limit (green line) together with the upper (black dashed line) and lower (blue dashed line) parameter boundary.

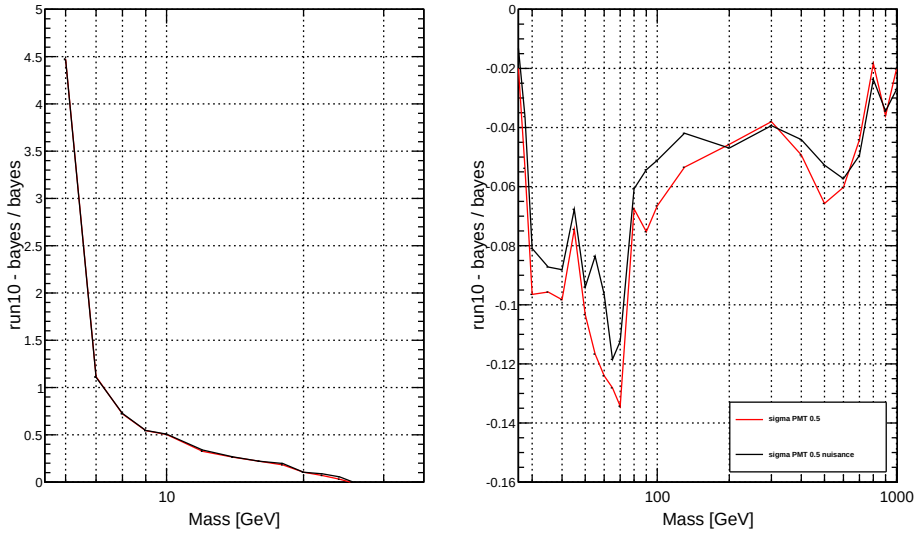

Figure 5.14.: Comparison of the Bayesian (blue line) and PL 225 live days limit for N_b as nuisance parameter. For direct comparison the difference of the limit with constant N_b (red line) is included.

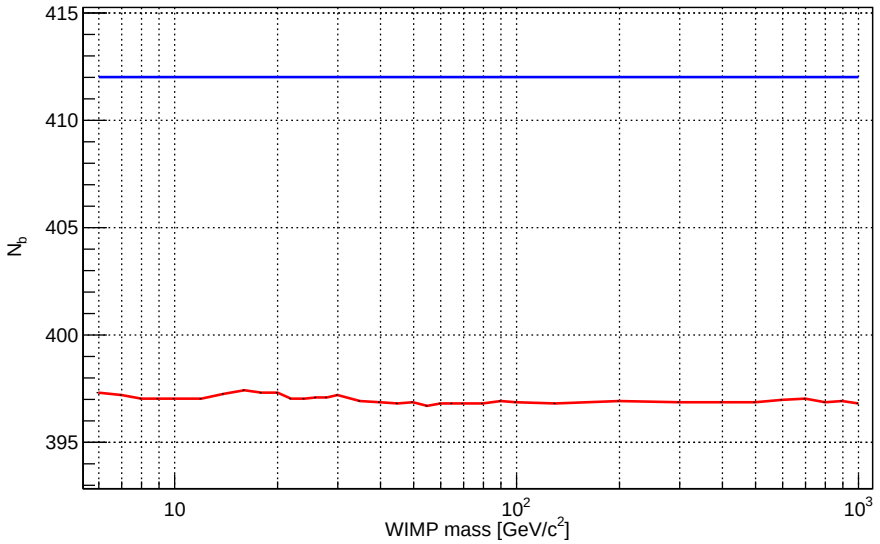

Figure 5.15.: Estimated amount of background events N_b (red line) compared to the constant value from the background model (blue line). Even if N_b is sampled independently for every mass the parameter stays constant.

5.3.3 Influence of the lower parameter range boundary

To check the influence on the choice of the parameter range a calculation for a different lower parameter boundary is done. Instead of assuming a flat lower parameter boundary at $1 \cdot 10^{-46}\,\mathrm{cm}^2$, the old limit of the XENON10 detector is divided by a constant factor of 10^4. Figure 5.16 shows the resulting limit together with the changed lower parameter range boundary. The default SPE resolution $\sigma_{PMT} = 0.5$ and no nuisance parameters were chosen. As in the studies before, in Fig. 5.17 the difference with respect to the 225 live days PL limit is shown. For better comparison the difference for a flat lower parameter boundary is also included.

There is a noticeable difference in the limit when comparing the different choices of the lower parameter boundary. The flat lower parameter boundary is more general instead of assuming a "limit like" one. The assumption is more biased, but since the shape of a limit should not change as it gets more constraining it is also not a completely random presumption. The change of the lower parameter range boundary plays only a minor role in this study so far.

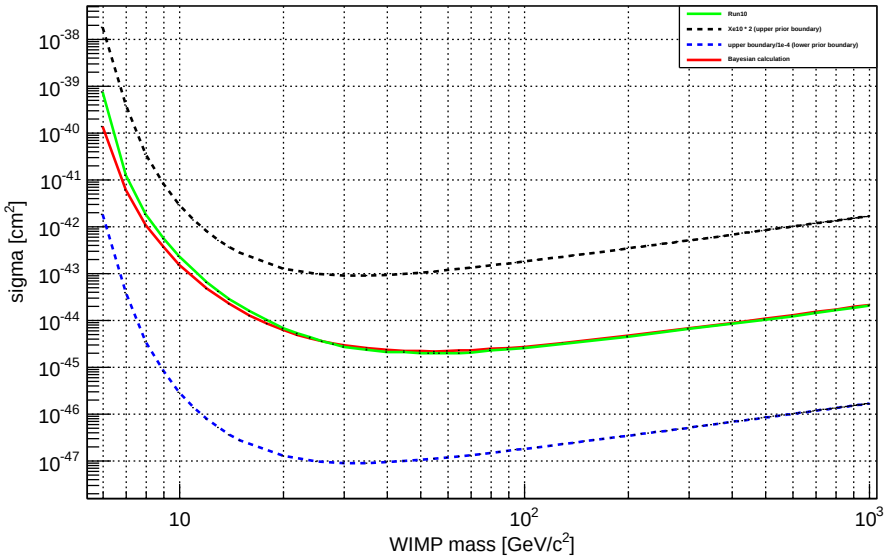

Figure 5.16.: Bayesian WIMP exclusion limit (red line) and PL 225 live days limit (green line) for a different choice of the lower parameter boundary (blue dashed line) together with the upper parameter boundary (black dashed line).

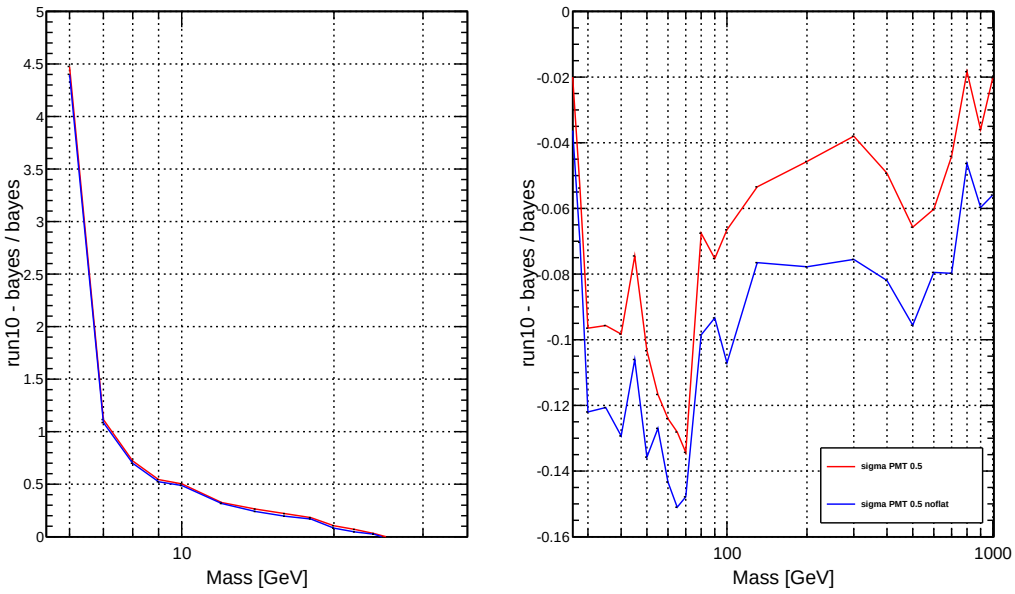

Figure 5.17.: Comparison of the Bayesian (blue line) and PL 225 live days limit for a different choice of the lower parameter boundary. For direct comparison the difference of the limit for a constant lower parameter boundary (red line) is included.

6 Conclusion and Outlook

After introducing the event rate calculation for the direct detection of WIMPs and studies on the average response width of the XENON100 Photomultiplier Tubes, the basic step towards a Bayesian analysis of XENON100 data was done in this work.

The average single photoelectron response σ_{PMT} was found to be higher, about 0.9 instead of 0.5, as the value gained from PMT LED calibrations. This was rather unexpected and is still under investigation. The impact on the calculated WIMP exclusion limit with Bayesian inference is rather small but noticeable. Since the differential energy rate spectrum becomes broader, for low WIMP masses an improvement of the obtained limit was observed. At higher masses, the limit becomes less constraining because of the slight decrease in the overall differential energy rate. Future tests with more light during the calibration or with different data sets will be done. Improving the model of the response could also be a possible task.

After gathering the ingredients needed for the analysis, like the event rate calculation and adopting the likelihood function from the PL analysis, a successful implementation into the Bayesian Analysis Toolkit was realized. The task to reproduce the well-established WIMP exclusion limit of the Profile Likelihood analysis was not completely achieved. There are still too many simplifications done in the new analysis. With the introduction of a nuisance parameter (total expected background events N_b), in most cases less constraining limit was obtained, which is closer to the 225 live days PL limit. As the main aspect of future investigations will not be the reproduction of an analysis that was already done, it is an intermediate step towards an independent and alternative approach for the analysis of XENON100 data.

The influence of a different choice for the parameter range showes a little impact on the calculated limit. Even if the flat lower parameter boundary is more general and less biased, the choice of a variable “limit like” lower boundary seems appropriate as it is an additional degree of belief which is put into the analysis.

After successfully introducing the rest of the nuisance parameters and uncertainties, the main task in the future will be to change the prior probability density function of the parameters of interest, not assuming a flat parameter distribution (like in the PL analysis) anymore.

During my studies to understand the model behind the detection in a Time Projection Chamber, developing a program for its analysis and exploring a new approach to statistics, a lot of new knowledge was gained by my side.

A Tables

A.1 Results of the maximum gap calculations

Table A.1.: Results of the maximum gap calculations.

WIMP mass [GeV]	σ [cm^2]	WIMP mass [GeV]	σ [cm^2]
6	$1.72{\cdot}10^{-40}$	50	$9.38{\cdot}10^{-46}$
7	$8.44{\cdot}10^{-42}$	55	$9.29{\cdot}10^{-46}$
8	$1.41{\cdot}10^{-42}$	60	$9.29{\cdot}10^{-46}$
9	$4.06{\cdot}10^{-43}$	65	$9.38{\cdot}10^{-46}$
10	$1.62{\cdot}10^{-43}$	70	$9.57{\cdot}10^{-46}$
12	$4.33{\cdot}10^{-44}$	80	$1.01{\cdot}10^{-45}$
14	$1.78{\cdot}10^{-44}$	90	$1.08{\cdot}10^{-45}$
16	$9.07{\cdot}10^{-45}$	100	$1.13{\cdot}10^{-45}$
18	$5.57{\cdot}10^{-45}$	130	$1.34{\cdot}10^{-45}$
20	$3.78{\cdot}10^{-45}$	200	$1.90{\cdot}10^{-45}$
22	$2.83{\cdot}10^{-45}$	300	$2.72{\cdot}10^{-45}$
24	$2.25{\cdot}10^{-45}$	400	$3.56{\cdot}10^{-45}$
26	$1.86{\cdot}10^{-45}$	500	$4.39{\cdot}10^{-45}$
28	$1.62{\cdot}10^{-45}$	600	$5.25{\cdot}10^{-45}$
30	$1.44{\cdot}10^{-45}$	700	$6.09{\cdot}10^{-45}$
35	$1.18{\cdot}10^{-45}$	800	$6.93{\cdot}10^{-44}$
40	$1.05{\cdot}10^{-45}$	900	$7.81{\cdot}10^{-44}$
45	$9.76{\cdot}10^{-46}$	1000	$8.63{\cdot}10^{-44}$

A.2 Results of the Bayesian calculations

Table A.2.: Results of the Bayesian calculations.

WIMP mass [GeV]	σ [cm^2]	WIMP mass [GeV]	σ [cm^2]
6	$1.37{\cdot}10^{-40}$	50	$2.22{\cdot}10^{-45}$
7	$5.96{\cdot}10^{-42}$	55	$2.23{\cdot}10^{-45}$
8	$1.07{\cdot}10^{-43}$	60	$2.25{\cdot}10^{-45}$
9	$3.59{\cdot}10^{-43}$	65	$2.28{\cdot}10^{-45}$
10	$1.52{\cdot}10^{-43}$	70	$2.34{\cdot}10^{-45}$
12	$4.83{\cdot}10^{-44}$	80	$2.47{\cdot}10^{-45}$
14	$2.21{\cdot}10^{-44}$	90	$2.63{\cdot}10^{-45}$
16	$1.25{\cdot}10^{-44}$	100	$2.75{\cdot}10^{-45}$
18	$8.44{\cdot}10^{-45}$	130	$3.30{\cdot}10^{-45}$
20	$6.16{\cdot}10^{-45}$	200	$4.64{\cdot}10^{-45}$
22	$4.92{\cdot}10^{-45}$	300	$6.72{\cdot}10^{-45}$
24	$4.16{\cdot}10^{-45}$	400	$8.73{\cdot}10^{-42}$
26	$3.58{\cdot}10^{-45}$	500	$1.09{\cdot}10^{-45}$
28	$3.23{\cdot}10^{-45}$	600	$1.30{\cdot}10^{-44}$
30	$2.97{\cdot}10^{-45}$	700	$1.49{\cdot}10^{-44}$
35	$2.55{\cdot}10^{-45}$	800	$1.68{\cdot}10^{-44}$
40	$2.34{\cdot}10^{-45}$	900	$1.92{\cdot}10^{-44}$
45	$2.24{\cdot}10^{-45}$	1000	$2.11{\cdot}10^{-44}$

B Code snippets

B.1 PMT response

This code snippet shows the implementation of the simulation for the PMT response as described in section 4.2.

```
void simulation(){
...
  for(int iter =0 ; iter<1000 ; iter++){ // 1000
    int n = 100 ; // iteration steps 100
      double ExpVal[n];
      double filler = 0;

      TH1F *his[100] ; // 100
      for(int hi=0 ; hi<100; hi++){ //100
        string his_name = GetString->int_to_string(hi)+"_"+GetString->int_to_string(iter);
        string nameh1 = "hist_";
        his[hi] = new TH1F( (nameh1+his_name).c_str(),"",2000, -0.05 , 199.95);

        filler = filler + 0.3 ;
        ExpVal[hi] = filler ;
      }

      double meanGaus = 1 ; // mean s.p.e
      double sigmaGaus = 0.9 ; // sigma s.p.e

      for (int i=0; i<100 ; i++){
      for(int j=0; j<100 ; j++){ // # entries per histogram
        double ngamma =  ExpVal[i];
              double NPE = gRandom->Poisson(ngamma);
              double gausionize = gRandom->Gaus(meanGaus*NPE,sqrt(NPE)*sigmaGaus);
              his[i]->Fill(gausionize);
      }
    }
  }
...
}
```

B.2 Snippets from maximum gap method

Below the implementation of the maximum gap algorithm (5.3) is shown.

```
...
// get boundaries and calculate events
double S1lo = hrates->GetXaxis()->FindBin(3.);
double S1hi = hrates->GetXaxis()->FindBin(30.);
double S1gaplo = hrates->GetXaxis()->FindBin(gErToS1->Eval(7.1));
double S1gaphi = hrates->GetXaxis()->FindBin(gErToS1->Eval(7.8));
double intrateS1gap = hrates->Integral(S1gaplo,S1gaphi,"width") ;
double intrateS1window = hrates->Integral(S1lo,S1hi,"width") ;
// 224.5 live days and 34kg LXe
double exposure = 224.5 * 34. ;

// start loop over sigma -----------------------------

// initialize values
int nnsS1 = 1; \ac{PMT} response
bool brS1 = true;
double sigmaS1 = sigma_ref;
// loop over S1
while( brS1 == true && nnsS1 < ns){
  // calculate events in whole enery window for cross section sigmaS1
  double nu = sigmaS1 / sigma_ref * intrateS1window * exposure ;
  // calculate events in maximum gap for cross section sigmaS1
  double x  = sigmaS1 / sigma_ref * intrateS1gap * exposure ;
  // calcuate biggest integer smapper than nu/x
  double j = 0.;
  if( x > 0){
    j = floor(\ac{PMT} responsenu/x);
  }else{
    j = 0;
  }
  // initialize C0 and calculate its value
  double C0 = 0. ;
  for(int g=0;g<=j;g++){
    double facG = TMath::Factorial(g) ;
    C0 += (((pow((g*x-nu),g))*(exp(-g*x)))/facG)*(1. + g/(nu-g*x)) ;
  }
  // end loop if C0 >= 0.9 and draw point for sigmaS1 into graph with ↩
      corresponding WIMP mass
  if(C0 >= 0.9){
    gexS1->SetPoint(m,m_d,sigmaS1*1.e-36);
    brS1 = false;
  }
  sigmaS1 += 0.01* sigmaS1 ;
  nnsS1++;
}
...
```

B.3 Snippets from BAT

The following code snippet shows an example for the implementation into the Bayesian Analysis Toolkit, which is described in section 5.2.4.

```
void xsec::DefineParameters(){
  // cross section range in pb
  AddParameter("sigma", 1.e-10 , grXe10_prior->Eval(Mass)/1.e-36 );
}

// ---------------------------------------------------------
double xsec::LogLikelihood(const std::vector<double> &parameters){
  // initialize log-likelihood
  double logprob = 0.;
  // Set sigma as parameter 0
  double sigma = parameters[0];
  // cross section range in pb
  double s1Min = 3;
  // upper threshold in p.e.
  double s1Max = 30;
  // # of bands
  static const int k = 12 ;
  double n[k];
  // read DM data from graph grDataband[ib] for band nb
  for(int ib = 0; ib < nb; ib++) n[ib] = grDataband[ib]->GetN();
  // expected background events in all bands from 3-30 pe
  double Nb = 412. ;
  // initialize signal events
  double Ms = 0;
  // declare array for signal events in the diffrent bands
  double ms[k];
  for(int ib = 0; ib < nb; ib++) {
    // # of all source events (NR calibration)
    Ms+= grAmBeband[ib]->GetN();
    // # of source events in band j
    ms[ib] = grAmBeband[ib]->GetN();
  }
  // initialize background events
  double Mb = 0.;
  // declare array for background events in the diffrent bands
  double mb[k];
  for(int ib = 0; ib < nb; ib++) {
    // # of all background events (ER calibration)
    Mb+= grCo60band[ib]->GetN();
    // # of background events in band j
    mb[ib] = grCo60band[ib]->GetN();
  }
  // reference cross section used to calculate WIMP spectra
  double xsec = 1.e-9 ;
  // exposre in days * kg
  double exposure = 224.561 * 34. ;
  // flat background spectrum
  double fb = 1./(s1Max-s1Min);
  // initialize variables
  double Ns= 0., s1= 0., s2= 0., es= 0., eb= 0., fs= 0. ;
  // calculate integral over differential rates
  double hisint = his.Integral( his.GetXaxis()->FindBin(s1Min) , his.GetXaxis()↩
      ->FindBin(s1Max) ,"width");
  for(int j =0 ; j < k ; j++){
```

```
54      // define probability for signal event to fall in band j
55      es = ms[j]/Ms ;
56      // define probability for background event to fall in band j
57      eb = mb[j]/Mb ;
58      // expected events
59      Ns =  sigma / xsec * hisint  * exposure ;
60      // # of expected events with cross section "sigma"
61      for(int i =1 ; i < n[j] ; i++){
62        // read s1 from data points i within band j
63        grDataband[j]->GetPoint(i,s1,s2) ;
64        if(hisint > 0)
65          // calculate normalized WIMP spectrum
66          fs =  his.GetBinContent(his.FindBin(s1)) / hisint ;
67        else
68          // check for the integral to be positive
69          fs = 0.;
70        // likelihood function
71        logprob += log(es*Ns*fs + eb*Nb*fb) + mb[j] * log(eb*Mb) + ms[j] * log(es↩
              *Ms) ;
72      }
73    }
74    // rest of likelihood function
75    logprob = logprob - Ns - Nb - Ms - Mb ;
76    // return the log probability of posterior
77    return logprob;
78  }
79
80  // ------------------------------------------------------------
81  double xsec::LogAPrioriProbability(const std::vector<double> &parameters){
82    // initialize log-likelihood
83    double logprob = 0. ;
84    // read parameter range
85    double dsigma = GetParameter(0)->GetRangeWidth() ;
86    // flat prior for sigma
87    logprob += log(1./dsigma) ;
88    // return the log probability of prior
89    return logprob;
90  }
91  // ------------------------------------------------------------
```

C Bibliography

[1] P.A.R. Ade et al. Planck 2013 results. XVI. Cosmological parameters. 2013. URL http://arxiv.org/abs/1303.5076.

[2] P.A.R. Ade et al. Planck 2013 results. XV. CMB power spectra and likelihood. 2013. URL http://arxiv.org/abs/1303.5075.

[3] *ROOT - An Object Oriented Data Analysis Framework*, September 1996. AIHENP'96 Workshop, Nucl. Inst. & Meth. in Phys. Res. A 389. URL http://www.sciencedirect.com/science/article/pii/S016890029700048X.

[4] E. Aprile et al. Likelihood Approach to the First Dark Matter Results from XENON100. *Phys. Rev. D*, 84:052003, 2011. URL http://arxiv.org/abs/1103.0303.

[5] E. Aprile et al. The XENON100 Dark Matter Experiment. *Astropart.Phys.*, 35: 573–590, 2012. URL http://arxiv.org/abs/1107.2155.

[6] E. Aprile et al. Analysis of the XENON100 Dark Matter Search Data. 2012. URL http://arxiv.org/abs/1207.3458.

[7] E. Aprile et al. Dark Matter Results from 225 Live Days of XENON100 Data. *Phys.Rev.Lett.*, 109:181301, 2012. URL http://arxiv.org/abs/1207.5988.

[8] E. Aprile et al. Response of the XENON100 Dark Matter Detector to Nuclear Recoils. 2013. URL http://arxiv.org/abs/1304.1427.

[9] J.D. Bekenstein, R.H. Sanders, J.D. Bekenstein, and R.H. Sanders. A Primer to Relativistic MOND Theory. *EAS Publications Series*, 20:225–230, 2006. ISSN 1638-1963. URL http://dx.doi.org/10.1051/eas:2006075.

[10] G. Bertone, D. Hooper, and J. Silk. Particle Dark Matter: Evidence, Candidates and Constraints. *Phys.Rept.405:279-390,2005*, August 2004. URL http://arxiv.org/abs/hep-ph/0404175v2;http://arxiv.org/pdf/hep-ph/0404175v2.

[11] W.M. Bolstad. *Introduction to Bayesian Statistics*. Wiley, 2007. ISBN 9780470181171. URL http://books.google.de/books?id=DzXaiLDTFS0C.

[12] T. Bruch, J. Read, L. Baudis, and G. Lake. Detecting the Milky Way's Dark Disk. *The Astrophysical Journal*, 696(1):920, 2009. URL http://stacks.iop.org/0004-637X/696/i=1/a=920.

[13] A. Caldwell, D. Kollár, and K. Kröninger. BAT – The Bayesian analysis toolkit . *Computer Physics Communications*, 180(11):2197–2209, 2009. URL http://www.sciencedirect.com/science/article/pii/S0010465509002045.

[14] A. Caldwell, D. Kollár, and K. Kröninger. BAT - The Bayesian analysis toolkit. *Computer Physics Communications*, 180:2197–2209, November 2009. URL http://adsabs.harvard.edu/abs/2009CoPhC.180.2197C.

[15] D. Clowe et al. A Direct Empirical Proof of the Existence of Dark Matter. *The Astrophysical Journal Letters*, 648(2):L109, 2006. URL http://stacks.iop.org/1538-4357/648/i=2/a=L109.

[16] J. Goodman et al. Constraints on dark matter from colliders. *Phys. Rev. D*, 82:116010, Dec 2010. URL http://link.aps.org/doi/10.1103/PhysRevD.82.116010.

[17] C. Grignon. Private communications. April 2013.

[18] Francis Halzen and Dan Hooper. The Indirect Search for Dark Matter with IceCube. *New J.Phys.*, 11:105019, 2009. URL http://arxiv.org/abs/0910.4513.

[19] W.K. Hastings. Monte Carlo sampling methods using Markov chains and their applications. *Biometrika*, 57:97–109, 1970.

[20] Richard H. Helm. Inelastic and Elastic Scattering of 187-Mev Electrons from Selected Even-Even Nuclei. *Phys. Rev.*, 104:1466–1475, Dec 1956. URL http://link.aps.org/doi/10.1103/PhysRev.104.1466.

[21] G. Hinshaw et al. Nine-Year Wilkinson Microwave Anisotropy Probe (WMAP) Observations: Cosmological Parameter Results. 2012. URL http://arxiv.org/abs/1212.5226.

[22] P. Konar. Shedding light on the dark sector with direct WIMP production. *New Journal of Physics*, 11(10):105004, 2009. URL http://stacks.iop.org/1367-2630/11/i=10/a=105004.

[23] H. Landsmann. Background model for the profile likelihood analysis. August 2012. URL https://xecluster.lngs.infn.it/dokuwiki/doku.php?id=xenon:xenon100:analysis:run10_profile_likelihood_summary#background_model.

[24] J.D. Lewin and P.F. Smith. Review of mathematics, numerical factors, and corrections for dark matter experiments based on elastic nuclear recoil. *Astroparticle Physics*, 6(1):87–112, 1996. URL http://www.sciencedirect.com/science/article/pii/S0927650596000473.

[25] Y. Mei. *Direct Dark Matter Search with the XENON100 Experiment*. PhD thesis, Rice University, April 2011. URL http://xenon.physik.uni-mainz.de/mainzTheses/Thesis_YuanMei201105.pdf.

[26] M. Milgrom. A modification of the Newtonian dynamics as a possible alternative to the hidden mass hypothesis. *Astrophysical Journal*, 270:365–370, July 1983.

[27] A. A. Penzias and R. W. Wilson. Determination of the Microwave Spectrum of Galactic Radiation. *Astrophysical Journal*, 146:666, December 1966. URL http://adsabs.harvard.edu/abs/1966ApJ...146..666P.

[28] D.H. Perkins. *Particle Astrophysics, Second Edition*. Oxford Master Series in Physics. OUP Oxford, 2009. ISBN 9780199545452. URL http://books.google.de/books?id=fBNzZF7kLz4C.

[29] G. Plante et al. New Measurement of the Scintillation Efficiency of Low-Energy Nuclear Recoils in Liquid Xenon. *Phys.Rev.*, C84:045805, 2011. URL http://prc.aps.org/abstract/PRC/v84/i4/e045805.

[30] V. C. Rubin and Jr. W. K. Ford. Rotation of the Andromeda Nebula from a Spectroscopic Survey of Emission Regions. *Astrophysical Journal*, 159:379, February 1970.

[31] P. Tisserand et al. Limits on the Macho Content of the Galactic Halo from the EROS-2 Survey of the Magellanic Clouds. *Astron.Astrophys.*, 469:387–404, 2007.

[32] L. Wyrzykowski et al. The OGLE View of Microlensing towards the Magellanic Clouds. III. Ruling out sub-solar MACHOs with the OGLE-III LMC data. 2010.

[33] S. Yellin. Finding an upper limit in the presence of an unknown background. *Phys. Rev. D*, 66:032005, Aug 2002. URL http://link.aps.org/doi/10.1103/PhysRevD.66.032005.

[34] Viktor Zacek. Dark Matter, July 2007. URL http://arxiv.org/abs/0707.0472.

[35] F. Zwicky. Die Rotverschiebung von extragalaktischen Nebeln. *Helvetica Physica Acta*, 6:110–127, 1933. URL http://adsabs.harvard.edu/abs/1933AcHPh...6..110Z.

[36] F. Zwicky. On the Masses of Nebulae and of Clusters of Nebulae. *Astrophysical Journal*, 86:217, October 1937. URL http://adsabs.harvard.edu/abs/1937ApJ....86..217Z.

List of Abbreviations

BAT	Bayesian Analysis Toolkit
CL	Confidence Limit
CMB	Cosmic Microwave Background
DM	Dark Matter
ΛCDM	Λ-Cold Dark Matter
LSP	Lightest Supersymmetric Particle
LXe	liquid Xenon
MACHO	Massive Astrophysical Compact Halo Object
MCMC	Markov Chain Monte Carlo
MOND	MOdified Newtonian Dynamics
pdf	probability density function
PL	Profile Likelihood
PMT	Photomultiplier Tube
PTR	Pulse Tube Refrigerator
RMS	Root Mean Square
SHM	Standard Halo Model
SPE	single photoelectron
SUSY	Supersymmetry
TPC	Time Projection Chamber
WIMP	Weakly Interacting Massive Particle

List of Figures

List of Tables

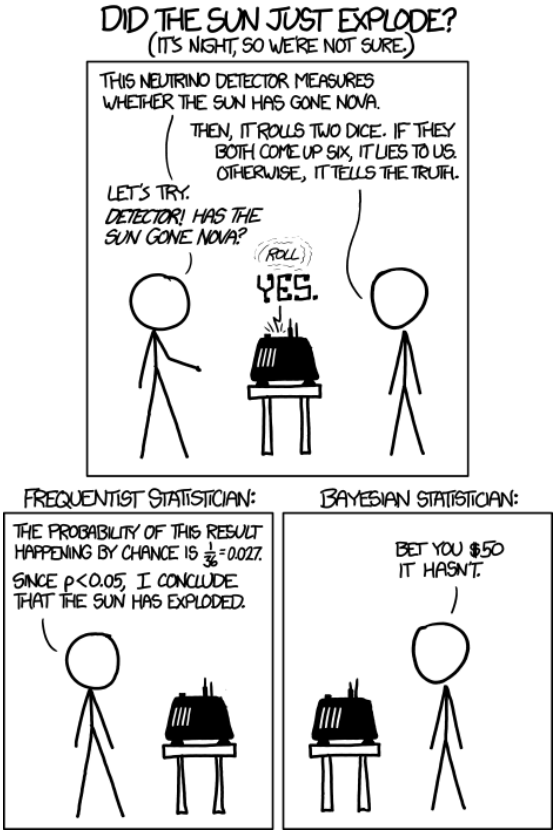

Bayesian vs. frequentist reasoning, a comic from xkcd (http://xkcd.com/1132/).

Erklärung zur Selbstständigkeit

Hiermit erkläre ich, dass die vorliegende Arbeit selbständig, ohne fremde Hilfe und ohne Benutzung anderer als die angegebenen Quellen von mir angefertigt wurde.

Mainz, den 04. Juni 2013

Stefan Schindler